Segmentation of Carpal Bones

using Statistical Shape Models based on Spherical Harmonics

C. Srinidhi Ragunathan









C. Srinidhi Ragunathan Graduate year 2019

Delft Institute of Technology

MASTER OF SCIENCE THESIS

Segmentation of Carpal Bones using Statistical Shape Models based on Spherical Harmonics.

Department of Biomedical Engineering and Physics

Academic Medical Center

Meibergdreef 9, 1105 AZ Amsterdam

Dr.G.Streekstra g.j.streekstra@amc.uva.nl

Dr.J.G.G Dobbe j.g.dobbe@amc.uva.nl

Dr.F.M.Vos f.m.vos@tudelft.nl

Contents

1	Introduction 1.1 Wrist Bone Segmentation	
2	Literature Review 2.1 Method of Search. 2.2 Texture Representation 2.2.1 Probabilistic Texture Representation 2.2.2 Wavelet based Texture Representation 2.2.3 Local Binary Patterns 1 2.3 Discussion 2.4 Conclusion 1	6 0 1 2
3	Methods 1 3.1 Model Building Process 1 3.1.1 3D Spherical Harmonic Shape Modelling (SPHARM) 1 3.1.2 Parametrization of a Shape Model 1 3.1.3 Shape Registration 2 3.1.4 Statistical Analysis 2 3.2 Segmentation Scheme 2 3.2.1 Model Initialization 2 3.3 Optimization 2 3.3.1 Pose Parameters 2 3.3.2 Shape Parameters 2	5 7 0 1 2 2 3 4
4	Experiments and Results 2 4.1 Dataset. 2 4.2 Experiments. 2 4.2.1 Model Complexity 2 4.2.2 Number of modes. 2 4.2.3 Gaussian Scale of Smoothing and Initial Step Size in LM algorithm. 2 4.3 Segmentation Evaluation 2 4.4 Results 2 4.4.1 Shape Optimization 3	7 7 8 8 9
	5.1 Analysis	5 6
Bi	liography 3	7

1

Introduction

With the recent advancements in processing tools for medical images, there is an increase in the quantitative analysis of these images in the clinical radiology and surgical domain. In the orthopedic field, Computer Assisted Orthopaedic Surgery (CAOS) and Computer Aided Diagnosis (CAD) started with the introduction of key technologies such as surgical robotics, patient specific templates and 3D bone surface modelling from CT images. The key-step at the basis of all image-based methods (CAD and CAOS) is image segmentation. For example, patient specific bone models are derived from image segmentation and surface mesh reconstruction. Such patient specific models are essential for preoperative planning, intra-operative registration, visualization and intra - operative navigation [1].

Image segmentation consists of partitioning an image into regions of interest, thus enabling to recognize, label and delineate critical organs and background tissues. The range of available segmentation methods vary from simple gray-level thresholding to complex deformable models such as level sets, active contours and active appearance models [2]. Despite years of research and advancement, efficient, automatic and robust segmentation is one of the main challenges that exists in computerized image processing. Furthermore, to this day, radiologists use manually segmented images as the ground truth for anatomical models. This process can be time-consuming, error prone due to intra- or inter - operator variability and demands expertise from highly trained personnel for reproducible results [3].

One such image segmentation scenario is the study of CT scans of wrist bones for diagnostic procedures. In this research, the endocrinological problems and growth disorders is investigated in children by analyzing the carpal bone structures [4]. Wrist bone segmentation also helps analyze and simulate complex wrist motion. This helps in detection of kinematic abnormalities caused by ligament rupture. An example is the research carried out by Van de Giessen *et al.* [5] where, the destabilization and abnormal motion of the wrist joint due to ligament tear was studied using a Local Statistical Shape Model (LSSM).

In section (1.1) the specific challenges posed by wrist bone segmentation will be addressed. In section (1.2), reasons for the basis of Statistical Shape Models as a solution strategy will be presented.

1.1. Wrist Bone Segmentation

Wrist bones are one of the most complicated structures (in terms of shape) in the skeletal system. The wrist consists of eight small, irregularly shaped carpal bones, two forearm bones and five metacarpal bones (Figure 1.1).

Bone segmentation in CT / X-ray images is assumed to be straightforward due to their high Hounsfield unit. However in case of carpal bones, the volumetric data sets contain irregularly shaped bones with small inter-bone distance, which proves to be challenging [7]. A key point to consider while analyzing bones, is their composition. Bone tissue material properties are not distributed uniformly. The cortical

1. Introduction

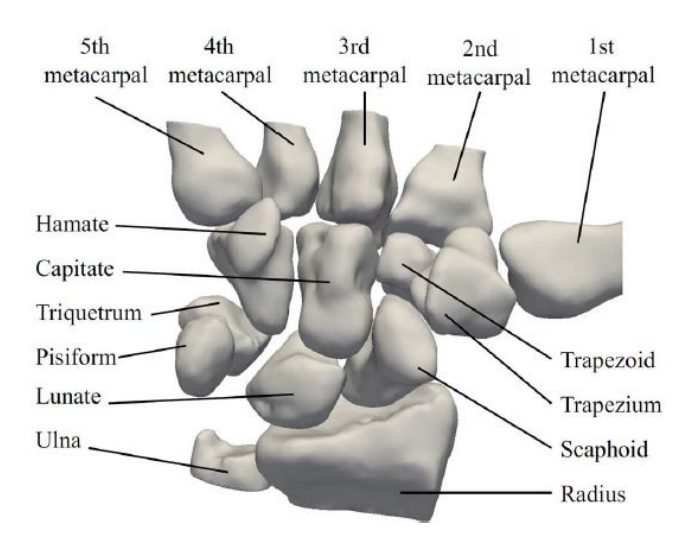


Figure 1.1: Schematic Diagram of the wrist bones [6].

layer or the outer layer is denser than the inner layer (spongy bone). Hence the texture in spongy bones can vary between tissue like intensity and bone like intensity. The close spacing between these bones and blurring of the CT image makes the inter bone space appear brighter compared to the background soft tissue [7].

1.2. Statistical Shape Models

Statistical Shape Models have been used for decades, for image analysis in the medical field [2]. Shape models must be in-variant to Euclidean similarity transformations (geometric, scaling and translation). Traditionally, the shape of any object is defined by a set of **n** 2D or 3D landmarks points (Points of correspondence on each object to match shapes within a population). Furthermore, landmarks can be classified into two categories, anatomical landmarks and mathematical landmarks. A major drawback of anatomical landmarks is that, the surgeon/ radiologist performing the marking has to pay attention to detail in order to have accurate correspondence between the shapes [8]. Mathematical landmarks are related to geometric properties of the shape, for example, a local high curvature.

Shape representation in the field of computer vision and image analysis was initial done using Level Sets by Malladi *et al.* [7]. Later, the most popular modelling technique has been variants of Active Shape Modelling (ASM) and Active Appearance Modelling (AAM) introduced by Cootes and Taylor [9]. ASM is a local search algorithm for identifying shapes, based on Point Distribution Model (PDM) where an instance of the model $\bf y$ in an image is defined by the mean shape $\bf x$ and shape parameter $\bf b$:

$$\mathbf{y} = \mathbf{x} + \phi \mathbf{b},\tag{1.1}$$

in which, $\phi = (\phi_1....\phi_c)$ is the matrix of eigenvectors. The eigenvectors represent the covariance matrix of the point distribution. From the initial shape and position, adjustments are calculated for each landmark by evaluating the fit of the shape at different points along the normal vector to the surface. Instead of a shape model, an appearance model which contains texture information as well, can be used for evaluating the fit. Model adjustments then lead to an optimal set of displacements. However, approaches based on PDM are time-consuming and tedious, requiring the user to manually place landmark points between sample images [8]. These pre-requisites prove to be challenging when dealing with complex, amorphous structures.

To overcome the need for correspondence between the training shapes, a landmark free shape modelling technique may be used. Spherical Harmonics, a spherical coordinate system based modelling

technique, overcomes this drawback. Spherical Harmonics (SPHARM) was used to conduct quantitative morphological assessment and image segmentation on brain structures, such as the hippocampus by Keleman *et al.* [10] and Styner *et al.* [11]. Parametric Deformable models have also been created using Spherical Harmonics for the purpose of Semi-Automatic Segmentation of the prostate by Tutar *et al.* [12]. Recently, a 3D spherical harmonics intensity model for 3D shape analysis of the Heterochromatin Foci was created by Eck *et al.* [13]. Here, a shape descriptor was defined based on the spherical harmonic coefficients and these were used as parameters to constrain the foci.

A literature review has been conducted in this study to investigate the effect of textures in conjunction with statistical shape models to improve a segmentation procedure. Each method has been briefly discussed along with the field in which they can be applied. The advantages and disadvantages of each method have also been enumerated.

In this project, the aim was to test the use of statistical description based on Spherical Harmonics to facilitate automated segmentation for analyzing bone structures for pre- and post- operative procedures. Therefore, the purpose of this thesis was to develop a framework based on Spherical Harmonics based Statistical Shape Modelling (SSM) to automatize the segmentation of carpal bones.

Literature Review

Precise segmentation of anatomical structures obtained from Computed Tomography images is of immense importance in the medical discipline. The result of segmentation is useful in post surgery assessment for example, in orthopaedic, oncological and neurological application [14]. It also supports in planning and image guidance for radiation therapy and surgery. For example, Wang *et al.* [15] present a method where the texture features are calculated by Random Forest (RF) Regression method and these features are used for segmenting the mandible and maxilla for the diagnosis and treatment of patients affected by craniomaxillofacial (CMF) deformities. Similarly, Chu *et al.* [16] presented a Fully Automated CT segmentation of the hip joint for computer assisted diagnosis and planning (CADP) of periacetabular osteotomy (PAO). They used an RF regression framework and in addition to it, used an improved fast Gaussian transform for landmark detection. They also used a Statistical Shape model for hip joint surface preservation.

Most radiologists prefer to use manually segmented images as the ground truth for anatomical models, though this process can be time-consuming and reproducible results can be obtained only after sufficient training. In the last decade, several automated methods of segmentation have been implemented in organ delineation, varying from simple gray-level thresholding to complex deformable models such as level sets, active contour and active appearance models. At the same time, segmentation is not a trivial task, owing to challenges like overlapping of pixel intensities and vague edges between the foreground and background [14]. In complicated scenarios such as wrist bones or the vertebral bone, simple morphological operations and local thresholding will fail in segmentation. Other limitations of CT images include low signal to noise ratio, inadequate spatial resolution (due to partial volume effect) and problems in separating bones present in close proximity. Additional issues arise when low intensity structures such as spongy bones (rib cage) need to be distinguished from background soft tissue.

The goal of this literature review is to present various ways in which texture can be presented or analyzed, to explore the possibility of incorporating texture into a statistical model framework and analyze its effect on improving the segmentation process. The review begins with the method of search used to access the research work carried out since 2011. Next, each method is briefly discussed, along with the field in which they have been applied. Finally, the advantages and drawbacks of all the methods will be compared and further investigate the possibility of incorporating it into a statistical model framework.

2.1. Method of Search

To search for relevant research work conducted, we started with two Database, **Web of Science** and **PubMed**. **Google scholar** and **ScienceDirect** did not give any other relevant results besides what was already found in PubMed and Web of Science.

As shown in Figure (2.1), two search cycles were conducted on **Web of Science**. In the first cycle, the keywords Segmentation, Appearance Representation and Statistical Model were entered. The first

6 2. Literature Review

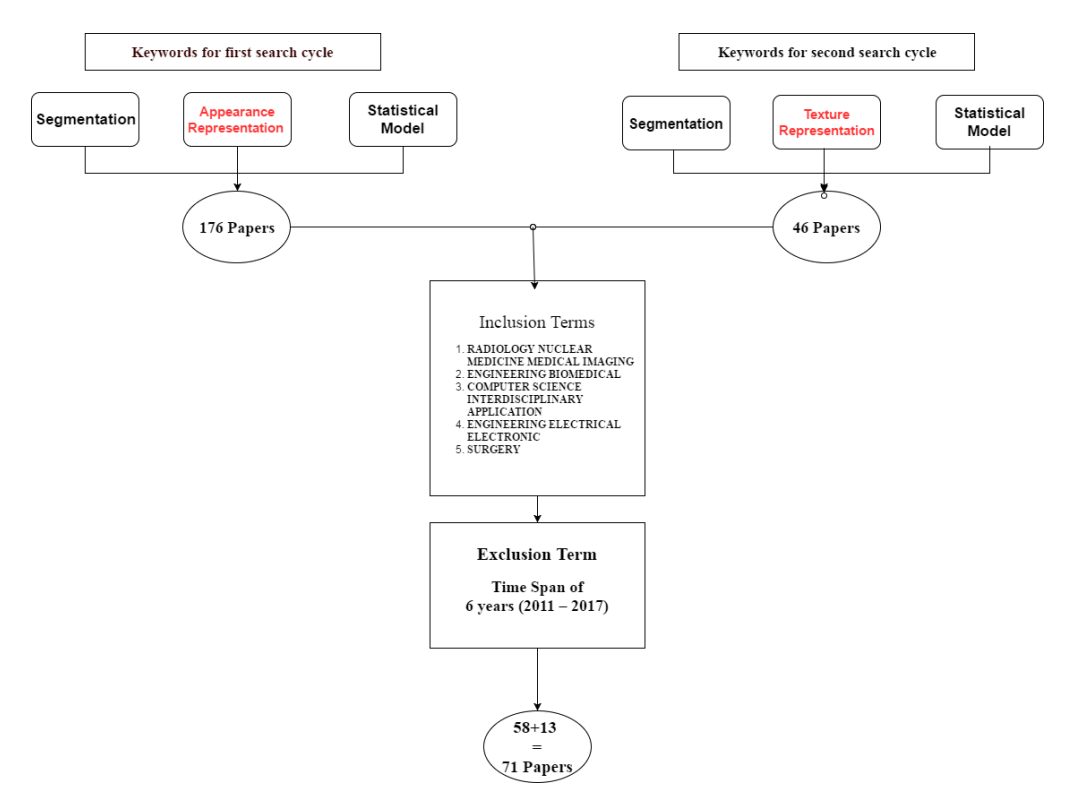


Figure 2.1: Search Term Flow Chart.

and the third term were used as the aim of the research is to segment an organ of interest using a statistical model. The second term stands for a model that contains both shape and appearance information. This search resulted in about 176 papers. To filter the results further, the inclusion and exclusion terms shown in Figure (2.1) were applied. This resulted in 58 papers. Research studies from these papers gave importance to various shape representation methods and only generic texture representation techniques were covered. Hence, a second search cycle was carried out, with the keyword "Texture Representation" in place of "Appearance Representation" to cover a narrow domain. The same filters as the previous cycle were applied to restrict the papers to medical imaging field. This resulted in a total of 13 papers. A total 71 papers were obtained.

After reading the above papers, not more than 10 papers deviated from the generic texture representation method. Also, some of the methods were used in conjunction with classifiers for segmentation and the validity of these texture representation methods with statistical or deformable models couldn't be found. The following works could be categorized under three broad topics, **Probability Based Texture Representation**, **Wavelet Based Texture Representation** and **Local Binary Patterns**. In the next section, each category will be discussed and their applications will be presented.

2.2. Texture Representation

2.2.1. Probabilistic Texture Representation

Automatic segmentation using Fuzzy Corners

Athertya *et al.* [17] conducted a study on how soft computing techniques can improve the performance of statistical shape models in the segmentation process of the vertebral bones. They applied an Active Contour Model (ACM) along with fuzzified edge intensities to delineate the vertebral bone. ACM, also known as, snakes are one of the earliest deformable models used for image segmentation. These models deform, to lock onto features of the test image and these features include lines, edges or object boundaries. The ACM algorithm deforms the points in the contour iteratively, approaching the object edge by minimizing the energy.

Fuzzy Logic, in a broader sense is synonymous with the concept of fuzzy sets, which relates to classes of objects with non-sharp boundaries. Fuzzy theory states that reasoning of a logical statement is not restricted to either true or false but can range from almost certain to highly unlikely. Fuzzy clustering is sub-topic of Fuzzy Logic, wherein a certain data point can belong to a cluster to some degree, which is a specified by a membership grade. Fuzzy clustering can be regarded as an adaptive thresholding method. This is because it uses the centroid of each class (where the classes are created based on the positions where maximum intensity pixels are present) of samples to adjust to the cost function. The fuzzy system identifies the intersection of ridges and valleys that constitutes a corner in the image and considers them as important features. In this research, a conventional Harris corner detector was applied to detect the corners of the region of interest. But along with the region of interest (ROI), stray boundaries, i.e. the corners of the soft tissues were also labelled as the boundary of the vertebral bone. This in turn compromised the contour evolution and the contour deviated away from the boundary of the ROI. Fuzzy Logic is used to identify true candidates, i.e. edges that can assist in contour evolution in the presence of high level of noise.

Here, a fuzzy corner metric that uses a fuzzified (application of a fuzzy membership function to crisp data) intensity mask on the corners detected by the Harris corner detector is used for identifying the candidate features. Let X be the fuzzy set consisting of image intensities x and be characterized by a continuum grade membership function $\mu(x)$ whose value ranges between 0 to 1. Specifically, an S type membership function (polynomial membership function) is employed for fuzzifying the crisp data (see Figure (2.2)). This type of membership function gives a higher weightage to pixels that have a higher intensity, thus aiding in segmentation of bones in CT images. Once the image is fuzzified, a threshold is set in order to extract the likely corner pixels.

$$\mathbf{S}(x;a,b) = \begin{cases} 0, & x \le a \\ 2\frac{(x-a)^2}{(b-a)^2}, & a \le x \le \frac{a+b}{2} \\ 1 - 2\frac{(x-a)^2}{(b-a)^2}, & \frac{a+b}{2} \le x \le b \\ 1, & x \ge b \end{cases}$$
 (2.1)

In equation (2.2), x is the input image intensity, a is the foot point b is the peak point and **S** is the fuzzified intensity. Here, a and b determine the extremes of the sloped portion of the curve. The fuzzified threshold intensity $\mathbf{t}(x)$ is given by

$$\mathbf{t}(x) = \begin{cases} S(x), & S(x) > th \\ 0, & S(x) \le th \end{cases}$$
 (2.2)

where, $\mathbf{t}(x)$ stands for the fuzzy threshold intensity, \mathbf{th} is the threshold intensity which is supposed to extract the top 90 percent of image features. This function is used as a mask for identifying the significant corner points. The weighted combination of suppressed corner strength with the fuzzy thresholded input image gives the fuzzy corners of the image (as shown in equation (2.3)).

$$\mathbf{C}(x) = \mathbf{t}(x) * \mathbf{C_r}(x) \tag{2.3}$$

Figure (2.2) is a graph of a typical S type membership function that was generated on MATLAB. Here, the membership function maps each element of the set X to a membership value between 0 and 1. The x axis of Figure (2.2) represents the input data, in our case the image intensities and the y axis represents the weights to be assigned to the input data.

Figure (2.3) shows a step wise conduction of the experiment. A Gaussian noise of mean 0 and variance beginning with a value of 0.01 and ending at 0.20 was added to the CT images. Harris Corner Detection , Global Thresholding and Fuzzy corner detection were applied on the noisy image. In Figure (2.3b) we can see that the corner points detected are not only those of the vertebral bone, but also those of the neighbouring soft tissues. But in Figure (2.3c), after application of Fuzzy metric the corners are present only on the vertebral bone. The results of the segmentation, carried out by various corner detection methods were then quantitatively analyzed using Dice similarity coefficient and the Hausdorff distance. The Harris detector completely fails in the segmentation process post noise addition, whereas the Fuzzy corner detection method has an error of about 0.7 at variance of about 0.20.

8 2. Literature Review

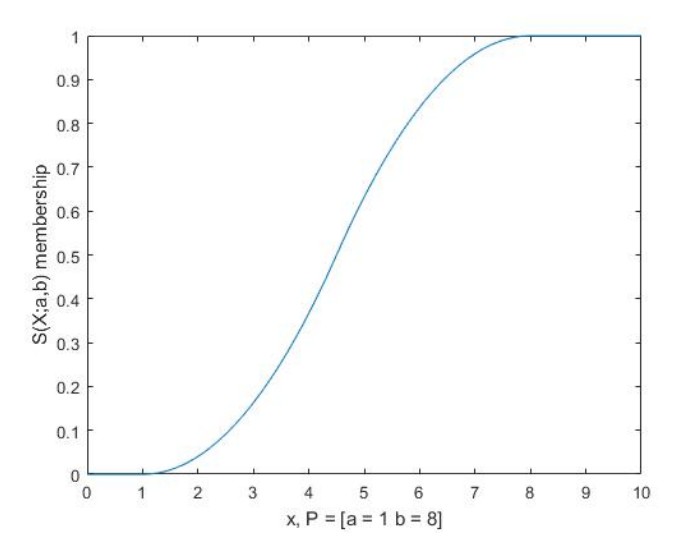


Figure 2.2: S Type Membership function.

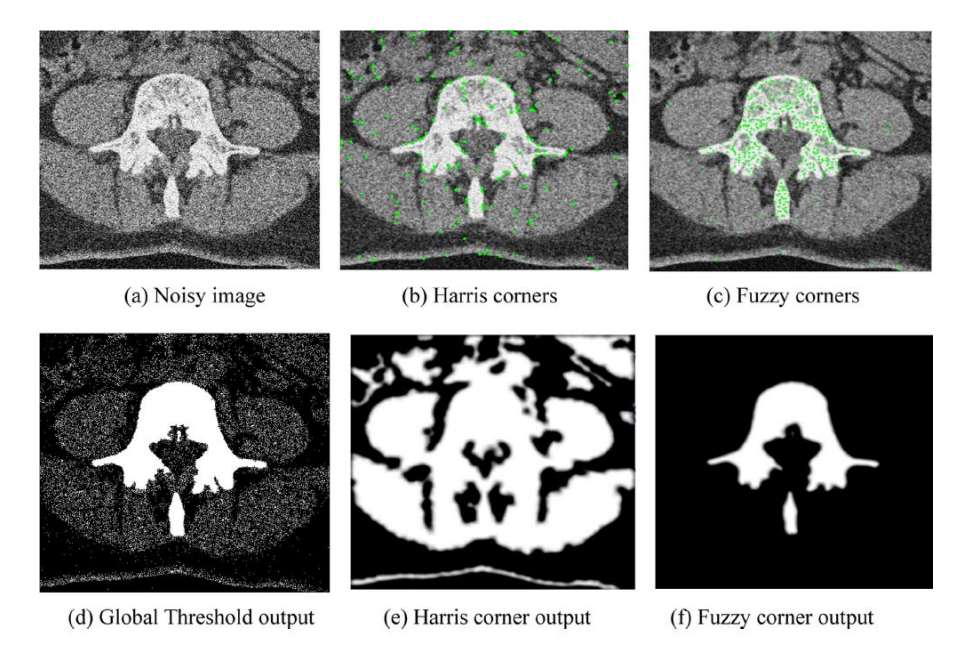


Figure 2.3: Application of Harris Corner Detection, Global Threshold and Fuzzy corner Detection on a noisy spine image. Image retrieved from [17].

Segmentation of CT imagery using Anatomical Constraints

- S. Chen *et al.* [18] have proposed a probabilistic method to overcome challenges faced by radiotherapists when it comes to segmentation of the prostate and the rectum for Intensity Modulated Radiotherapy. Two major difficulties faced during the segmentation process are:
 - 1. The minimal intensity difference between the prostate, rectum and surrounding muscles.
 - 2. Intensity distribution of the rectum varies due to filling of gas, causing inadequacies during segmentation.

S.Chen *et al.* [18] proposed retaining the training segmentation's gray level histogram as a basis of learning the accurate distribution of the intensities inside and outside the desired shape for the test image. These histograms are then incorporated into a Bayesian framework and the distance (Euclidean) between the reference histogram and test image histogram is treated as the cost function. The intention is to find an index of similarity between the test image and the training image. The distance between any two histograms can be expressed in terms of the distances of element measurement values. Given two sets of n elements, A and B, we consider the problem as one of finding the minimum difference of pair assignments between two sets. The problem is to determine the best one-to-one assignment between two sets such that the sum of all differences between two individual elements in a pair is minimized [19]. Along with the intensity cost, a shape and anatomical position cost function is also included to aid in cleared segmentation.

Initially, a statistical shape model (based on [9]) is created by applying Principal Component Analysis (PCA) on surface polygon.

$$S^{\beta} = S' + P\beta \tag{2.4}$$

Here, S^{β} is the new shape and β is the parameter that produces different instances of the shape. Now, in the Bayesian framework, the problem is to find a new shape instance β' based on the training images. The intensity information of the target image is characterized corresponding to a given β value. This is done using the histogram intensity values inside the organ of interest h_{in} , intensity outside the organ h_{out} and intensity in the entire domain h_{en} . h_{in} and h_{out} are functions of β and the relation between the three terms are as follows:

$$h_{en} = \alpha h_{in} + (1 - \alpha) h_{out} \tag{2.5}$$

Here, α denotes the ratio between the volume inside the organ to the volume of the entire domain and volume denotes the total number of intensity pixels in the region. The histograms learned from the training image are given by \tilde{h}_{in} , \tilde{h}_{out} and \tilde{h}_{en} for the internal intensity, external intensity and the entire domain's intensity respectively.

The intensity cost is finally modelled as shown in equation (3.6):

$$p(h_{in}(\beta), h_{out}(\beta), h_{en}|\tilde{h}_{in}, \tilde{h}_{out}, \tilde{h}_{en}) = p(\alpha(\beta)|\tilde{\alpha}) * p(h_{in}(\beta)|\tilde{h}_{in}) * p(h_{out}(\beta)|\tilde{h}_{out})$$
(2.6)

The Bayesian framework is described as follows: Probability of estimating the different instances of the target organ as a function of its inner pixel intensity and as a function of the intensity outside the chosen organ, given the internal composition of grey level, external composition of grey level intensities and the gray level composition of the entire chosen domain computed from the training images can be determined by the probability of estimating the organ instance (β) as a function of the volume of the image intensities, the intensity inside the organ and the intensity outside the organ.

They model $p(\alpha(\beta)|\tilde{\alpha})$ as a 2-D Gaussian distribution and the densities of the prostate and rectum is estimated using the 2D kernel density. In both cases, a 2D estimate is calculated as the segmentation is carried out in a slice-wise manner.

The output of the statistical segmentation is compared to the organs manually segmented by the physician. They concluded that, the current framework is found to be robust to noise and initialization of the shape and intensity model. However, when the intensity distribution of the rectum and prostate

2. Literature Review

overlap, some regions of the bladder is also segmented along with the prostate. The research also shows that, the anatomical position and the shape of the bladder has maximum positive effect on segmentation.

2.2.2. Wavelet based Texture Representation

Statistical characteristics of Gabor based filters have often been used for Face Recognition systems. Y. Ge. *et al.* [20], proposed the use of the mean of Gabor Magnitude and Phase over varying scales and directions. Gabor based filters are represented by a plane wave or a sinusoidal wave enveloped by a Gaussian Function as shown in equation (2.7).

$$h(x,y) = s(x,y)g(x,y)$$
(2.7)

The sinusoidal wave is given as in equation (2.8)

$$s(x,y) = e^{-j2\pi(u_0x + v_0y)}$$
 (2.8)

and g(x,y) represents the Gaussian envelope in equation (2.9),

$$g(x,y) = \frac{1}{\sqrt{2\pi\sigma}} e^{-\frac{1}{2}(\frac{x^2}{\sigma_x} + \frac{y^2}{\sigma_y})}$$
 (2.9)

and the direction of the texture is given as,

$$\theta = tan^{-1} \frac{u_0}{v_0} \tag{2.10}$$

The Gaussian function dictates the scaling property of the Gabor function. The direction in which the frequencies of the texture are measured is controlled by the plane/sinusoidal wave. The scale is denoted by σ the direction by θ . In equation (2.10), u_0 and v_0 are referred to as the spatial frequencies. Thus, the Gabor function can be thought of as a Gaussian function that is shifted in frequency space by u_0 and v_0 . Altering σ , changes the space/image area over which the texture is being analyzed. This Gabor function is convolved with the image to obtain the Gabor Magnitude and Phase. Usually, the Gabor Magnitude features are preferred over the Gabor Phase features, as the Gabor magnitude, which is known to vary slowly with the spatial position, the Gabor phase can take very different values even if it is sampled at image locations only a few pixels apart. This fact makes it difficult to extract stable and discriminative features from the phase response.

Y. Ge. *et al.* [20], used the Gabor function to extract the facial textures for face recognition purpose. These features were then concatenated into a single matrix, and substituted the local gray level profiles in an Active Shape Model. However, this lead to increased storage and longer computation time as the size of the Gabor textures were 40 times that of the gray level intensities. So, to compensate for this, three simplified representations of the Gabor features were suggested. First, the mean of the Gabor Magnitude and Phase over the scales where calculated (CGMPS). Next, the mean of the same features over varying direction were calculated (CGMPD). Finally the mean of the features over both the scales as well the directions were calculated (CGMPSD).

The proposed approach was compared to sigmoidal normalization of the gradient (SGrad) of the pixels. The SGrad at each pixel can be expressed as given in equation (2.11).

$$g_n = \frac{(g_x, g_y)^T}{|g| + \bar{g}}$$
 (2.11)

Here, |g| denotes the magnitude of the gradient normalized by the sigmoidal function, (g_x, g_y) is the gradient of the pixel and \bar{g} is the mean of |g|.

Two quantities of the segmented images were analyzed. First the accuracy i.e. how well the model fit, was compared in all four cases. In this case, the sigmoidal normalized gradient gave the performance while the mean of Gabor features over both scale and direction performed the worst. The metric used

to calculate the performance was point to point error between the model and manually labelled points. Second, the effect of size on the storage and the speed of the system were analyzed. In this case, the mean of the Gabor features over scale and mean of Gabor feature over the directions fared better in comparison to the sigmoidal normalized gradient.

It was inferred from this experiment that, computational efficiency of the Active Appearance Model can be significantly increased, by condensing the number of intensity features. Secondly, they have also concluded that this method makes the segmentation process invariant to illumination and change in facial expression.

2.2.3. Local Binary Patterns

The Local Binary Pattern (LBP) operator is an efficient texture descriptor, which is highly discriminative and has proven to be invariant to monotonic gray level changes. This operator was proposed by Ojala *et al.*[21] based on the idea that surface structures can be defined by two measures, local spatial patterns and gray level contrast. The original LBP operator used a 3x3 mask to describe the neighbourhood around the pixel of interest. The gray level intensity of the neighbourhood pixel is compared with the central pixel, and is assigned a value 0, if less than the central pixel value else a value 1. Then an 8-bit LBP code for a neighborhood is formed. The decimal value of this binary code gives the local structural information around the given pixel [22]. The histogram of these $2^8 = 256$ different labels can then be used as a texture descriptor.

The LBP expression is given as in equation (2.12):

$$LBP(x) = \sum_{p=0}^{P-1} s(g_{x_i} - g_x) 2^i$$
 (2.12)

where s(z) is defined as in equation (14):

$$s(z) = \begin{cases} 1, z \ge 0, \\ 0, z < 0 \end{cases}$$
 (2.13)

In equation (2.12), g_{x_i} is the location of the i_{th} neighbouring pixel, g_x is the central pixel and g is the intensity at those pixel positions. By applying this procedure we form an LBP image which has pixel values ranging between 0 and 255. Every LBP value corresponds to a different pattern. The histogram of these images show how often each LBP repeats itself in a given texture. This operator can be further extended to different scales, by adopting a circular geometry. The local neighbourhood is defined as set of sampling points evenly spaced on a circle, whose centre is placed at the pixel to be labelled. Further, bi-linear interpolation is used when a sampling point doesn't fall at the center of the pixel. The notation (P, R) is used for the pixel neighbourhood notation, P stands for the number of sampling point and R for the radius of the circular patch[23].

While using LBP to analyze the texture of a surface, some important parameters need to be chosen to optimize the performance. These include, the type of LBP operator chosen and the number of regions into which the image has been divided.

Gonzaleza *et al.* [24] conducted a research on the different segmentation techniques for Knee cartilage segmentation. They combined Active Shape Models by [9] and two different types of LBP operators: generic LBP and median-LBP. In the median-LBP, the central pixel is replaced by median of itself and the P surrounding neighbours.

$$LBP_{P,R}^{med}(x_c, y_c) = \sum_{p=0}^{P-1} s(g_p - \bar{g}),$$
 (2.14)

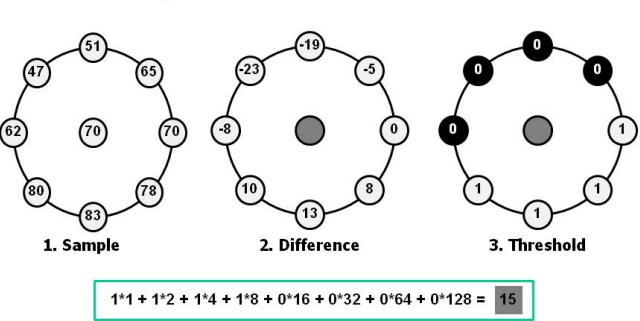
where \bar{g} represents the median of the intensity values of the P neighbours and the central pixel. This operator is less sensitive to noise and is also rotation invariant.

Figure (2.5) shows the local texture histogram calculation using an LBP operator for the cartilage. The results of the segmentation, like in the case of the spinal segmentation was validated using the DICE coefficient and Hausdorff Distance (determines the similarity between any two shapes). Also, different

12 2. Literature Review

The value of the LBP code of a pixel (x_c, y_c) is given by:

$$LBP_{P,R} = \sum_{p=0}^{P-1} s(g_p - g_c) 2^p \qquad s(x) = \begin{cases} 1, & \text{if } x \ge 0; \\ 0, & \text{otherwise.} \end{cases}$$



4. Multiply by powers of two and sum

Figure 2.4: An example of circular computation [24].

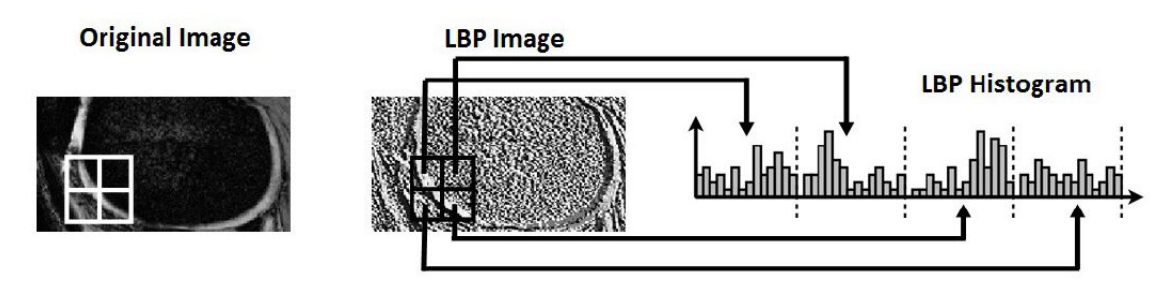


Figure 2.5: Local texture representation from sub-region histograms of the knee cartilage. Image obtained from [24].

Radii values (R=1, 2, 3, 5, 10 in pixels) were tested with the same number of neighbourhood points, in order to determine the best cartilage descriptor. Using the DICE coefficient and Hausdorff distance, that came to the conclusion that for R=1 and P=8, the best segmentation results were obtained and close behind it came the Median LBP operator for R=2 and P=8. The ASM-MLBP is shown to provide a better segmentation compared AAM, due to the pixel level information provided by the LBP descriptor, spatial information from sub-regions histograms and a global information from the concatenated LBP histogram.

2.3. Discussion

In this review, three methods of texture representation have been discussed briefly. The aim of our project is to segment the carpal bones, in specific the scaphoid and we have chosen Spherical Harmonics to be the choice of statistical shape model. The scaphoid is rather irregular in shape and presence of other irregularly shaped bones of similar intensity makes it a challenging task to segment them. Key points for choosing the optimal method for texture representation are features which would capture maximum information of the organ but at the same time will be storage efficient and computationally inexpensive. The other criteria is methods that are invariant to the presence of noise or illumination and assist the shape model in accurate initialization. Table (2.1) gives a brief scoring of each paper for the above mentioned criteria. The traditional method that is Active Shape model and Active Appearance model (as elaborated in section 1.2) has also been included in the table. + denotes if the given method exhibits the given feature and the – denotes the lack of feature. However, not all the methods that have been discussed elaborate on the necessary key points.

We can infer from the traditional texture representation that the accuracy of the method highly depends on the anatomical location of the organ, type of imaging protocol used and how precisely the

2.4. Conclusion

Key Criteria					
Feature	Traditional	Gabor Func-	Fuzzy Corner	Intensity	LBP
	Rep.	tion		Constraint	
Storage Efficiency	-	+	+	N/A	N/A
Computation Speed	+	+	+	N/A	+
Illumination Invari-	-	+	N/A	N/A	+
ance					
Noise Invariance	-	+	+	+	N/A
Model Initialization	-	N/A	+	+	N/A

Table 2.1: Scores for each method based on key criteria.

landmarks have been detected, as those locations are sampled to obtain the pixel intensities. AAM also suffers from low accuracy and weak robustness, which can be of a disadvantage when it comes to variation in illumination.

From the work carried out by [17], it can be inferred that use of Fuzzy logic to identify strong corners and edges based on the intensity can also help in accurate initialization of the statistical shape model. The Active Contour Model used in their experiment, segmented the vertebral bone accurately even in the presence of noise, when combined with the fuzzy corners, in comparison to Global Thresholding and use of a basic Harris corner Detector.

The use of a Gabor function to represent the texture information proved to be successful under different types of illumination. Another advantage of this method is, use of the mean value of the Gabor features proved to improve the run time of the segmentation process. It proves to be less expensive on the storage system when compared to using the Gabor Texture features alone (explained in section 2.2.2). Also, Gabor features can provide information of anatomical structure alignment, depending on the frequency of the textures. However, it is better to use the mean of the Gabor features than the output of the convolution itself, as the Gabor features are also high dimensional.

The Anatomical and intensity based constraints applied in the segmentation of prostates and rectum proved to be efficient. However, almost the entire segmentation process was guided by the anatomical positions and the shape constraints in comparison to the intensity cost. S. Chen *et al.* [18] suggested taking the intensity cost of other neighbouring structures such as the vertebral bone as well as the bladder to improve the segmentation process.

Use of Local Binary Pattern, has again widely been used for facial segmentation for face recognition and in one case, for extracting the knee cartilages. The main advantage of LBP as a texture descriptor is, it's tolerance to monotonic gray scale changes. Similar to other methods, it is computationally efficient. In comparison to the traditional way of representing the texture, there is no need for gray scale normalization while using LBP operator. Apart from the above mentioned clinical problems, LBP has also been used to characterize the Bone Mineral Density in osteoporosis patients.

2.4. Conclusion

Keeping in mind the key criteria for segmenting the carpal bones, we can conclude that the fuzzy logic based texture representation and the Gabor function, in the mentioned order can be adapted to segment the scaphoid. Owing to the irregular structure of the vertebral bone and the presence of soft tissues with a similar tissue composition in the neighbourhood, the Fuzzy Corner metric can be adapted to segment the scaphoid. The Gabor function can also be considered, given its use of direction of orientation as a feature to represent the textures. Little can be inferred from the segmentation using Anatomical Constraints. From the conclusions given by the authors, more weightage is given to the anatomical cost and the shape cost, over the intensity cost. But since this method has been applied to organs that have similar or same textured neighbours, it might be possible to adapt it for the scaphoid as well, as the neighbouring bones are in close proximity and are of similar intensity.

Methods

This chapter will focus on the model building process (section (3.1)) and the optimization method used for segmenting the image (section (3.2)). In Figure(3.1), we can see the flow of each subtopic. The idea is to first focus on model building and then understand the theory behind the segmentation process.

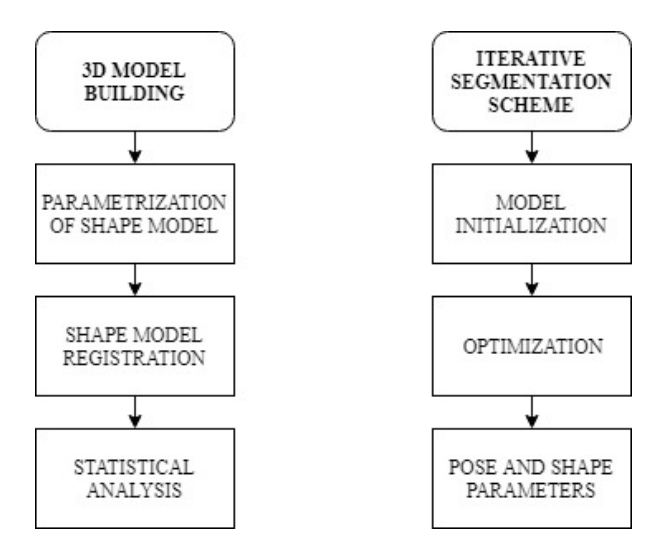


Figure 3.1: SSM building and application work-flow.

3.1. Model Building Process

3.1.1. 3D Spherical Harmonic Shape Modelling (SPHARM)

SPHARM, as the name suggests, is based on a spherical coordinate system. The data used to build this model will be described in detail in section 4.1. As shown in Figure (3.2), $\bf r$ is the distance from the origin to any point on the region of interest, the inclination angle ϕ , is the angle between the positive $\bf r$ axis and orthogonal projection of the line segment $\bf r$ on the x-y plane. ϕ varies between angles 0 and 2π . The azimuthal angle θ , is the angle between the z-axis and the line joining the origin and the point. θ varies from 0 to π [25].

The relation between Spherical and Cartesian Coordinate system is given by:

$$x = \rho sin\theta cos\phi \tag{3.1}$$

$$y = \rho sin\theta sin\phi \tag{3.2}$$

$$z = \rho \cos \theta \tag{3.3}$$

3. Methods

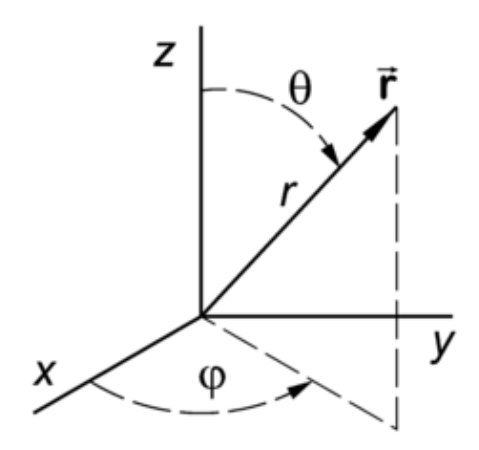


Figure 3.2: Spherical Coordinate System [26].

Spherical Harmonics use frequency-space basis functions to define shapes of spherical topology. SPHARM forms a complete set of basis functions defined over a sphere, which enables spherical functions to be expanded into a series of weighted harmonics [13]. The complex valued SPHARM basis function is defined as:

$$Y_l^m(\theta,\phi) = N_l^m * P_l^m(\cos\theta) * e^{im\phi}, \tag{3.4}$$

$$P_l^m = \begin{cases} (-1)^m (1 - x^2)^{(m/2)} d^m / (dx^m) P_l(x) & \text{if } m > 0\\ (-1)^m \frac{(l-m)!}{(l+m)!} P_l^{-m}(x) & \text{if } m < 0 \end{cases}$$
(3.5)

$$P_l(x) = \frac{1}{2^l l!} \left(\frac{d^l}{dx^l} (x^2 - 1)^l \right)$$
 (3.6)

$$N_l^m = \sqrt{\frac{2l+1}{4\pi} \frac{(l-m)!}{(l+m)!}}$$
 (3.7)

where, P_l^m is the associated Legendre Polynomial, $P_l(x)$ is the unassociated Legendre polynomial and N_l^m is a normalization coefficient.

In the above equations, I stands for the degree and m stands for the order of the basis function. The variable I represents the number of local minima of the function or the lower frequency information of the image. As the value of I increases, the shape can become more intricate. Since when building a statistical model real geometric objects are considered, equation (3.4) will be replaced by real valued spherical harmonics (equation (3.8)).

$$Y_{l}^{m}(\theta,\phi) = \begin{cases} \sqrt{2}N_{l}^{m}P_{l}^{m}cos(\theta)cos(m\phi), & \text{if } m > 0\\ N_{l}^{0}P_{l}^{0}(cos\theta) & \text{if } m = 0\\ \sqrt{2}N_{l}^{|m|}P_{l}^{|m|}cos(\theta)sin(|m|\phi), & \text{if } m < 0 \end{cases}$$
(3.8)

The shape vectors are chosen such that the SPHARM basis functions are orthonormal with respect to θ and ϕ . The general assumption is that the bone is star shaped, i.e. any point x_0 in the bone exists

such that each ray originating from x_0 intersects the surface only once. The other assumption is, the centre of the surface is a point x_0 and defines the outer surface to be a 3D radial function r [13], which is then written as a SPHARM expansion:

$$r(\theta,\phi) = \sum_{l=0}^{\infty} \sum_{m=-l}^{l} c_l^m * Y_l^m(\theta,\phi)$$
 (3.9)

where $c_l^m=(c_0^0,...,c_\infty^\infty)$ is the vector of expansion coefficients or the weights of the SPHARM basis functions and $r(\theta,\phi)$ represents the radius. Since SPHARM is orthonormal in nature, obtaining the coefficients c_l^m of n points from equally sampled surface representation $(r(\theta_l,\phi_l))$ and a SPHARM expansion of L_{max} can be treated as a Least Square Function (LSF) problem.

$$\begin{pmatrix} YLM_{1}(\theta_{1},\phi_{1}) & YLM_{2}(\theta_{1},\phi_{1}) & \dots & YLM_{k}(\theta_{1},\phi_{1}) \\ YLM_{1}(\theta_{2},\phi_{1}) & YLM_{2}(\theta_{2},\phi_{2}) & \dots & YLM_{k}(\theta_{2},\phi_{2}) \\ YLM_{1}(\theta_{n},\phi_{n}) & YLM_{2}(\theta_{n},\phi_{n}) & \dots & YLM_{k}(\theta_{n},\phi_{n}) \end{pmatrix} \begin{pmatrix} c_{1} \\ c_{2} \\ c_{k} \end{pmatrix} = \begin{pmatrix} r(\theta_{1},\phi_{1}) \\ r(\theta_{2},\phi_{2}) \\ r(\theta_{n},\phi_{n}) \end{pmatrix}$$
(3.10)

In equation (3.10), $YLM_j(\theta_n, \phi_n)$ is the linear form of the SPHARM basis function $Y_l^m(\theta, \phi)$, c_{xj} is the linear form of the weighting coefficient c_l^m , $k = (L_{max} + 1)^2$ and a unique indexing $j = l^2 + l + m + 1$ is used for each pair (l, m). In case of a 3D training image, a total of $3(L_{max} + 1)^2$ coefficients will be obtained [27].

3.1.2. Parametrization of a Shape Model

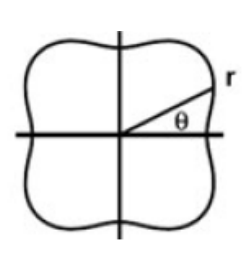


Figure 3.3: A simple 2D contour [28].

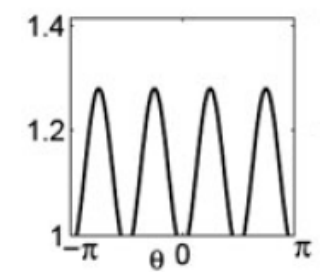


Figure 3.4: Mapping of the radius from the origin of the contour [28].

A simple 2D contour, specifically the one shown in Figure (3.3) can be represented by a standard Fourier series. A simple contour can be described using the radius as a function of the angle in the polar coordinate system θ . This function $r(\theta)$ maps a certain distance from the origin to specified points on the contour (Figure (3.4)).

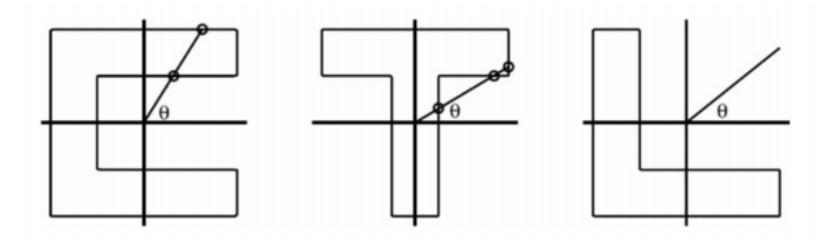


Figure 3.5: 2D contours that cannot be represented by radius function [28].

However, not all shapes lend themselves well to Fourier based representation. Given the bone of our choice, by definition, does not have star shaped geometry, the radius from the centre of mass will

3. Methods

cross the contour at more than one value for multiple values of θ . An example for the 2D scenario is shown in Figure (3.5). In case of the first and the third shape, the radius will not cross the contour at certain angles.

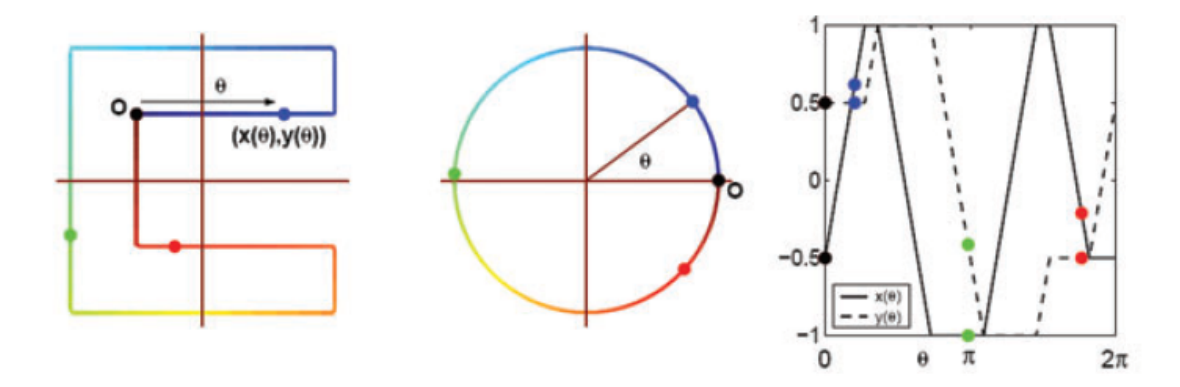


Figure 3.6: 2D Parametrization [28].

To overcome this issue, parametric functions can be employed to expand Fourier representation for complex surfaces. Parametrization simply refers to mapping of the object coordinates onto a unit circle/unit sphere. Two functions $x(\theta)$ and $y(\theta)$ parametrize the contour as a function θ , and in this case, θ is the arc length along the contour (Figure (3.6)). These two functions can then be broken down into a Fourier series. For the purpose of our study, this method will be extended to encompass closed 3D surfaces. As seen in Figure (3.7**B**) a closed 3D surface, which can be parametrized by $r(\theta,\phi)$. Analogous to the 2D scenario, the angular parameters in $r(\theta,\phi)$ correspond to an equal area on the surface. Using bijective mapping, the surface measurements are mapped on to a unit sphere, during which the purpose is to preserve the area of the object [28].

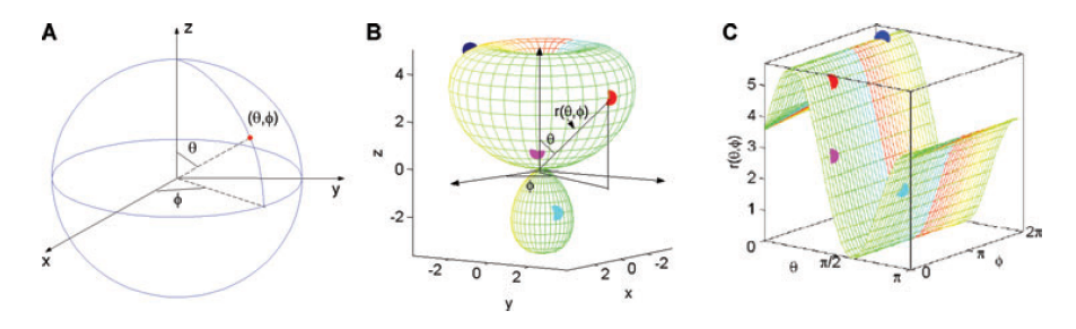


Figure 3.7: 3D Parameterization [28].

However, the process of mapping is not straightforward and minimization over some measure of distortion is required. Traditionally, the coordinates are mapped from the Cartesian coordinate system to the Polar coordinate system. However, this is applicable only for star shaped objects. Since most biological objects have either intrusions or protrusions, a new method called Control of Area and Length Distortion Algorithm (CALD) spherical parametrization has been introduced by Shen et.al [29]. This algorithm attempts to produce minimal angular and length distortion in simple connected triangular meshes while mapping the surface coordinates to a sphere. These triangular meshes consist of vertices (dense sampling of points over the image surface) and faces created by connecting the points.

The method proposed by Shen et. al. represents function $r(\theta, \phi)$ as $(x(\theta, \phi), y(\theta, \phi), z(\theta, \phi))$. This helps in separating the geometrical information in the object space from the parametrization in the parametric space. Given, a triangular mesh $M = \{t_i\}$, ψ is a continuous and invertible map, which

maps the triangular mesh M onto another mesh, $\psi(M) = \psi(t_i)$. Let A(.) denote the area of a triangle or a mesh. Then, the area distortion cost (ADC) \mathcal{C}_a for a each triangle t_i w.r.t. ψ , is:

$$C_a(t_i, \psi) = \frac{A(\psi(t_i))}{A(t_i)}$$
(3.11)

In the subsequent steps, the area distortion cost for triangles incident on each vertex is calculated. The goal of this framework is to find a mapping such that the area distortion cost of the entire mesh M is minimized:

$$C_a(M, \psi) = \frac{\sum_{t_i \in M} max\left(C_a(t_i, \psi), \frac{1}{C_a(t_i, \psi)}\right)}{A(\psi(M))}$$
(3.12)

The stretch concept introduced by Sander et al. is employed in this study. They consider the case of a mapping $\Psi:(s,t)\in R^2\to (x,y,z)\in R^3$ from a planar domain to a 3D surface. At any point (s,t), the singular values Γ and γ of the 3x2 Jacobian matrix $J_{\Psi}[d\Psi/ds,d\Psi,dt]$ represent the largest and smallest length distortions (called stretches) for each triangle t_i when mapping a vector from 2D to 3D surface.

$$C_s(M, \psi) = \sqrt{\frac{\sum_{t_i \in M} \left(\Gamma^2(t_i) + \frac{1}{\gamma^2(t_i)}\right) A(\psi(t_i))}{2A(\psi(M))}}$$
(3.13)

In the preliminary phase of parametrization, the two parameters θ and ϕ , are distributed over the surface S to form the mapping $\psi(M)$. $\theta \in [0,\pi]$ is taken as the co-latitudinal coordinate and $\phi \in [0,2\pi)$ is taken as the azimuthal coordinate. The north pole $\theta=0$ and south pole $\theta=\pi$ on the unit sphere are chosen such that their projections on the principle axis of inertia are furthest apart. Next two linear systems are solved, in order to get the θ and ϕ value for each point on the sphere.

After the mapping is determined, the next step is composed of local and global smoothing of the triangular meshes. Mesh smoothing involves movement of the vertices of the triangle on the surface of the sphere such that the initial parametrization quality is improved without disturbing the overall topology. The overall algorithm combines the local and global smoothing steps and each one is performed alternatively until the solution is achieved.

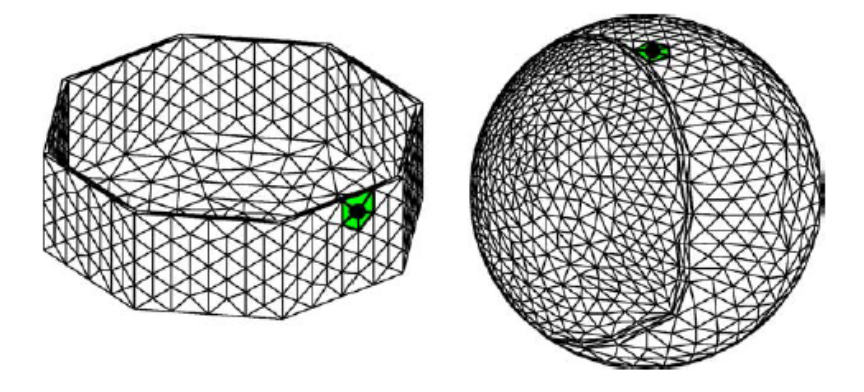
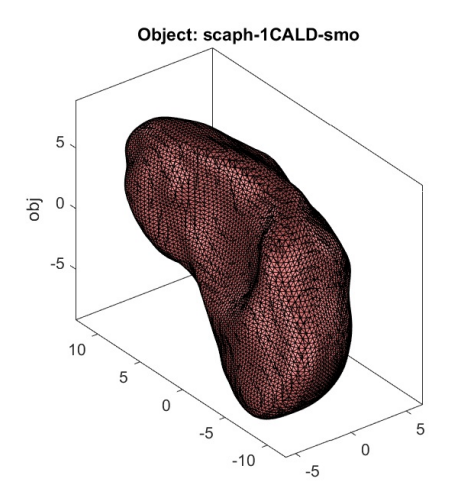


Figure 3.8: Example local submesh indicated in green color on both the object mesh on the left and spherical mesh on the right [28].

20 3. Methods

1. During local smoothing, an iterative loop is used, to traverse the entire spherical mesh in order to reduce the area distortion cost. At each iteration, the quality of the mapping is improved, by adjusting the position of the vertex of a submesh (Figure(3.8)), consisting of the elements incident on that vertex.

Given, a fine resolution mesh was used in the study by Shen et.al [29], each of the spherical submesh is assumed to be piece-wise linear in nature and hence can be projected onto a 2D plane. Subsequently, the projection preserves the relative area of each triangle on the parameter submesh. Given a flexible vertex v_0 to adjust and $v_i = (x_i, y_i)$ on the spherical submesh, the area A of the triangle consisting of these three vertices must be replaced by A_{ideal} (which is the area of the corresponding triangle on the object submesh). Subsequently, linear system is created in which the variables to be adjusted are the coordinates of the originally chosen vertex, i.e. the parameter submesh center, in order to minimize the square sum of the relative area of all the triangles of the submesh, while keeping the total area of the parameter submesh fixed.



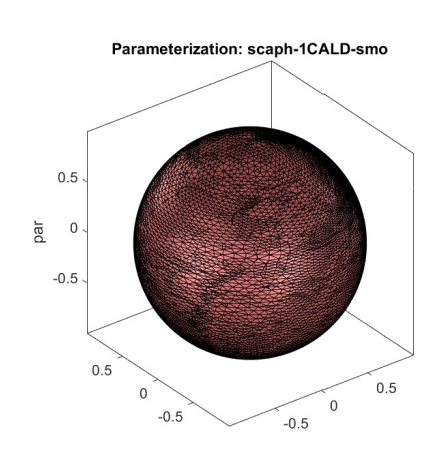


Figure 3.9: Parametrization in the object space.

Figure 3.10: Parametrization in the parameter space.

2. On the global scale, the distribution of area distortion cost over the entire sphere is calculated and tentatively equalized [27]. Figure (3.9 - 3.10) is an example of the parametrization of the scaphoid in object space and the parameter space.

At the local level, the area distortion cost is minimized by solving a set of linear equations, in which the variables that need to be adjusted are the coordinates of the vertex chosen in the first step (parameter submesh center). This is done, in order to minimize the square sum of the relative area difference of all the triangles of the sub-mesh, while keeping the total area of the parameter sub-mesh fixed. Shen et.al [29] performed one step of global smoothing and and n=10 steps of local smoothing until a stop criterion was achieved. The iteration stops when the average distortion has a minimum value of one (which is when the spherical harmonic expansion is one at every location of the unit sphere) and doesn't change for three iterations.

3.1.3. Shape Registration

In order for corresponding coefficients in two objects to be comparable, the SPHARM models of these objects must be placed in common reference system. Surface registration becomes a mandatory step when it comes to shape modelling. It is crucial to remove the effects of translation, scaling and rotation. In this project, one type of alignment approaches, First Order ellipsoid (FOE) has been used to do so.

FOE

The first order ellipsoid is used as an initial registration template in the parameter space and this is taken as the input for the second step, during which the registration is iteratively improved. For l=1,

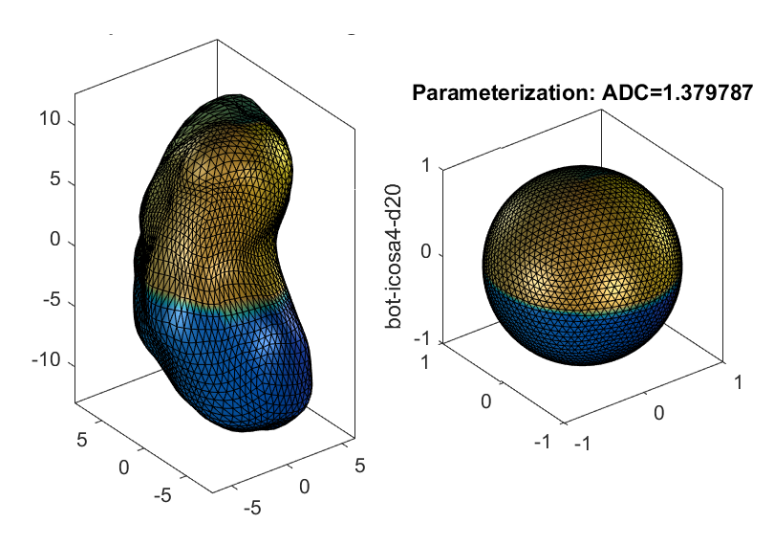


Figure 3.11: FOE alignment.

the SPHARM basis function is an ellipsoid for any training shape. The required landmarks are found by fitting the ellipsoid to the geometrical shape i.e., the north pole is at one end of the longest main axis, and the crossing point of the zero meridian and the equator is at one end of the shortest main axes. Figure (3.11) shows the image of a training shape in the object space and its corresponding parametrization in the parametrized space.

3.1.4. Statistical Analysis

Once the registration of the shape models is complete, the next step is to employ a statistical tool to study the multidimensional variations of the shape vectors of the training objects. Here, statistical tools such as Principal Component Analysis (PCA) have been applied to highlight the differences and similarities in the data set. Assuming the data has a Gaussian distribution, the mean shape of the point cloud can then be described as an average over s shapes:

$$\bar{x} = \frac{1}{n} \sum_{i=1}^{s} x_i \tag{3.14}$$

In case of spherical harmonics, taking the principal of orthonormality into consideration, the coordinates x_i are replaced by the spherical harmonic coefficients c_k .

$$\bar{c} = \frac{1}{n} \sum_{k=1}^{s} c_k \tag{3.15}$$

where \bar{c} is the mean of the shape coefficients. PCA consists of computing the covariance matrix S of the spherical harmonic coefficients and determine its eigenvalues and eigenvectors, defined as:

$$S = \frac{1}{n-1} \sum_{k=1}^{n} (c_k - \bar{x})(c_k - \bar{c})^T$$
 (3.16)

The eigen decomposition of the matrix S gives us the eigenvector matrix Ψ_n (eigenvectors) and their corresponding eigenvalues λ_n . Essentially, the directions of variation are described by the eigenvectors. The corresponding eigenvalues denote the variance in the given direction. The direction of variation are also termed as 'modes of variation' of the SSM. Modes of variation with higher variance describe bigger part of the total shape variation between given objects [5].

$$c_k = \bar{c} + \Psi * b_{ki} \tag{3.17}$$

22 3. Methods

$$c_{k} = \bar{c} + \begin{pmatrix} \Psi_{11} & \Psi_{12} & \dots & \Psi_{1(s-1)} \\ \Psi_{21} & \Psi_{22} & \dots & \Psi_{2(s-1)} \\ \Psi_{m1} & \Psi_{m2} & \dots & \Psi_{m(s-1)} \end{pmatrix} \begin{pmatrix} b_{k1} \\ b_{k2} \\ b_{k(s-1)} \end{pmatrix}$$
(3.18)

Since the eigenvectors are orthogonal and hence statistically independent, each shape c_k , can be represented as a linear combination of the column vector Ψ_n of the eigenvector matrix and the shape parameter vector b_{ii} as given in equations (3.17-3.18).

3.2. Segmentation Scheme

As explained in the introduction, one of the primary applications of building statistical models is to carry out segmentation of medical images. Here, segmentation is done by elastically fitting the shape model to a new 3D data set (refer to Flowchart in Figure (3.1)). This is achieved by the following two steps:

- Model Initialization by transforming the model coordinate system into that of the new data set.
- 2. Optimization: Elastic deformation is carried out it until cost function is maximized.

3.2.1. Model Initialization

Initially, rigid registration of the scaphoid model to the target CT volume was required to prevent the model based registration from converging into a local minima.

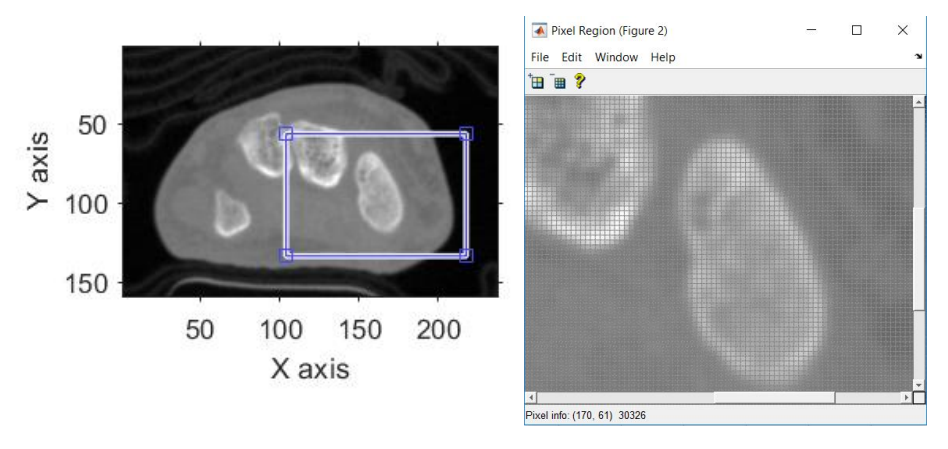


Figure 3.12: Slice Selection.

Figure 3.13: Selecting Threshold Value.

In order to make the process less cumbersome, a framework was created to extract the bone volume. A rough segmentation of the test image was carried out using OTSU thresholding to segment the wrist from the background tissue. OTSU thresholding chooses the threshold that minimizes the intra-class variance of the thresholded black and white pixels (Figure (3.12 - 3.13)) [30]. Next, a 2D slice lying in the range of the scaphoid length was selected. In the selected slice, each bone was color coded and labelled (Figure (3.14)).

The correct label corresponding to the scaphoid was then selected by the user and an inbuilt function **isosurface** was applied to extract the surface contour of the test volume.

The principal axes of inertia for the two objects, the roughly segmented volume and the mean model were then calculated using eigen-decomposition of the moments of inertia matrices of the bone meshes. Since the segmented volume and mean model are present in different coordinate systems, it is necessary to carry out Coordinate system transformation prior to initialization. Here, the 3D CT test image's coordinate system is used as reference.

$$M3 = M2 * M1^{-1} (3.19)$$

3.3. Optimization 23

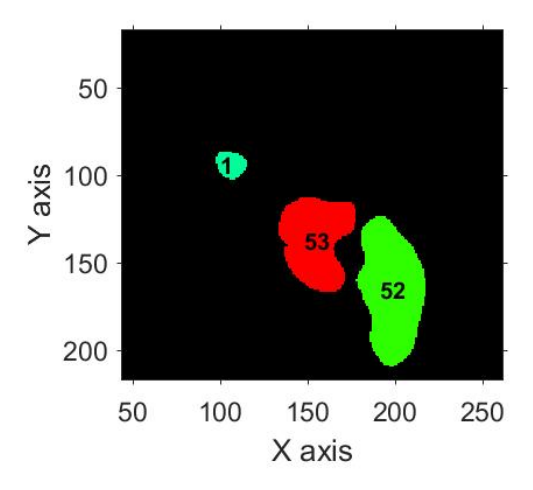


Figure 3.14: Colour coded and Labelled Image.

where, M2 is the inertia matrix of the segmented volume, $M1^{-1}$ is the inverse of the inertia matrix of the mean model and M3 is resulting the transformation matrix for aligning the mean model to the segmented volume.

3.3. Optimization

Before beginning the optimization procedure, a Gaussian filter is applied to blur the new gray level image and \vec{G} is calculated by applying a first order gradient to the new image. The primary goal is to obtain translation, rotation and shape parameters that maximize the inner dot product of the surface normal \vec{N} of the mean model and the gradient vector \vec{G} of the gray level image.

The metric to be optimized can represented as:

$$P(\vec{\theta}, \vec{t}, \mathbf{b}) = |\vec{N} \cdot \vec{G}| \tag{3.20}$$

where, $\vec{\theta}$ is the set of rotation parameters, \vec{t} is the translation parameters and **b** is the shape parameters.

The Levenberg Marquardt (LM) or the damped least square method has been used for obtaining the optimal pose and shape parameters. Since the LM algorithm solves for minimization of a non-linear least square problem, we take the final metric to be the negative of the dot product [31].

The LM algorithm is a blend of the steepest descent and Gauss Newton algorithm. It tends to perform a combined training process i.e., in areas with complex curvature the algorithm switches to the steepest descent method, until the local curvature is proper to make a quadratic approximation; then it approximately becomes the Gauss–Newton algorithm, which can speed up the convergence significantly[31].

Given a least square curve fitting problem, with a set of m data pairs, we need to estimate the parameters **B** so that $S(\mathbf{B})$ is minimized:

$$S(\mathbf{B}) = \sum_{i=1}^{m} [y_i - f(x_i, \mathbf{B})]^2$$
 (3.21)

With respect to our problem, **B** represents the pose parameters $\vec{\theta}$, \vec{t} and the weight vectors \vec{b} , y_i is the gradient vector \vec{G} and x_i is the surface normal N of the mean model. The LM algorithm is an iterative procedure, where the parameter vector **B** is replaced by a new estimate **B** + δ in every step. δ is calculated by approximating linearization of $f(x_i, \mathbf{B} + \delta)$:

$$f(x_i, \mathbf{B} + \delta) = f(x_i, \mathbf{B}) + J_i \delta \tag{3.22}$$

24 3. Methods

where, I is the Jacobian matrix, containing the gradient of the the shape model with respect to **B**.

$$S(\mathbf{B} + \delta) = \sum_{i=1}^{m} (y_i - f(x_i, \mathbf{B}) - J_i \delta)^2$$
 (3.23)

Taking the derivative of $S(\mathbf{B}, \delta)$ with respect to δ and setting the result to 0 gives us:

$$(J^{T}J)\delta = J^{T}[y - f(\mathbf{B})] \tag{3.24}$$

The above equation can also be represented as a damped version,

$$(J^{T}J + \lambda I)\delta = J^{T}[y - f(\mathbf{B})] \tag{3.25}$$

where the scalar, non negative value λ is the damping factor. λ controls the magnitude and direction of the step δ , with higher values of λ quickening the convergence. When λ is equal to 0, the algorithm behaves like the Gauss Newton method. As λ tends to infinity, the step δ tends towards the steepest descent method.

In section 3.3.1 and 3.3.2, the parameters to be optimized using LM will elaborated.

3.3.1. Pose Parameters

After initialization, the shape model first undergoes a geometric transformation, with a fixed scaling value and iteratively calculation of the rotation and translation parameters. A 3D body can be translated by some scalar t_x , t_y , t_z using:

$$(x, y, z) \to (x + t_x, y + t_y, z + t_z)$$
 (3.26)

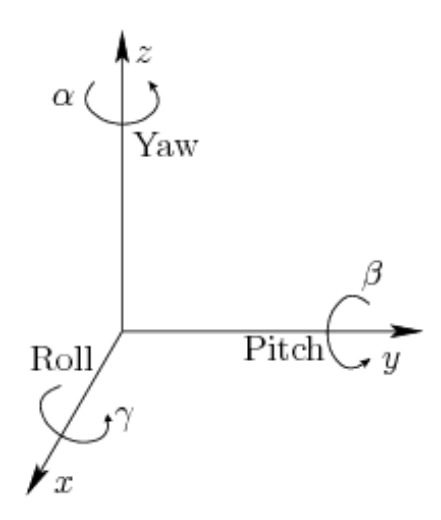


Figure 3.15: 3D rotation[32].

and can be rotated about its 3 orthogonal axes, where the angles are represented by the terms yaw, pitch and roll. Yaw or rotation in a counterclockwise direction of α about the z axis is given as

$$R_{z}(\alpha) = \left\{ \begin{array}{ccc} \cos(\alpha) & -\sin(\alpha) & 0\\ \sin(\alpha) & \cos(\alpha) & 0\\ 0 & 0 & 1 \end{array} \right\}$$
(3.27)

A pitch is a counterclockwise rotation of β about the y axis:

$$R_{y}(\beta) = \begin{cases} \cos(\beta) & 0 & \sin(\beta) \\ 0 & 1 & 0 \\ -\sin(\beta) & 0 & \cos(\beta) \end{cases}$$
 (3.28)

3.3. Optimization 25

A roll is a counterclockwise rotation of γ about the z axis:

$$R_{\chi}(\gamma) = \left\{ \begin{array}{ccc} 1 & 0 & 0 \\ 0 & \cos(\gamma) & -\sin(\gamma) \\ 0 & \sin(\gamma) & \cos(\gamma) \end{array} \right\}$$
(3.29)

The yaw, pitch and roll can be combined together in one single matrix. However, an order of multiplication has to be followed while combining the matrices. The conventional order to follow is $R_z(\alpha)R_v(\beta)R_x(\gamma)$.

$$R(\alpha, \beta, \gamma) = \begin{cases} \cos(\alpha)\cos(\beta) & \cos(\alpha)\sin(\beta)\sin(\gamma) - \sin(\alpha)\cos(\gamma) & \cos(\alpha)\sin(\beta)\sin(\gamma) + \sin(\alpha)\cos(\gamma) \\ \sin(\alpha)\cos(\beta) & \cos(\alpha)\sin(\beta)\sin(\gamma) + \sin(\alpha)\cos(\gamma) & \cos(\alpha)\sin(\beta)\sin(\gamma) - \sin(\alpha)\cos(\gamma) \\ -\sin(\beta) & \cos(\beta)\sin(\gamma) & \cos(\beta)\cos(\gamma) \end{cases}$$

$$(3.30)$$

The transformation matrix is a combination of the two parameters mentioned above.

$$T(\vec{\theta}, \vec{t}) = \left\{ \begin{array}{ccc} \cos(\alpha)\cos(\beta) & \cos(\alpha)\sin(\beta)\sin(\gamma) - \sin(\alpha)\cos(\gamma) & \cos(\alpha)\sin(\beta)\sin(\gamma) + \sin(\alpha)\cos(\gamma) & t_x \\ \sin(\alpha)\cos(\beta) & \cos(\alpha)\sin(\beta)\sin(\gamma) + \sin(\alpha)\cos(\gamma) & \cos(\alpha)\sin(\beta)\sin(\gamma) - \sin(\alpha)\cos(\gamma) & t_y \\ -\sin(\beta) & \cos(\beta)\sin(\gamma) & \cos(\beta)\cos(\gamma) & t_z \\ 0 & 0 & 1 \end{array} \right\}$$

$$(3.31)$$

The angles α, β, γ are the Euler angles that are obtained from the transformation matrix M3 (refer to equation 3.19). The vector $\bar{\theta}$ represents these angles and the vector \bar{t} represents t_x, t_y, t_z .

3.3.2. Shape Parameters

The pose parameters and the shape are optimized separately in this project. Since the shape model coefficients are affected by variance in rotation, after the first step of optimization, an inverse of the transformation matrix (equation (3.31)) T^{-1} is applied to the image. Next, the weight vectors b defining the shape can be optimized in a manner similar to the transformation parameters. The weight vector b is initialized to zero and the size of this vector is determined by the number of modes being taken into consideration.

The parameters of the shape model to be optimized are the spherical harmonic coefficients. To do so, At each iterative step, the dot product of the surface normal and the image gradient determine the updated value of the weight vector.

To describe legitimate shapes, a bounding condition for the weights **b** is applied. This range is usually $[-3\sigma, +3\sigma]$, where σ is the square root of the variance. It is not necessary to use all the modes of variation to describe the shape. The first k modes can be chosen, for example, 90% of them to incorporate the high frequency information.

Experiments and Results

4.1. Dataset

The dataset comprised of 20 scaphoids, obtained from the 3D CT scan of the right wrist of healthy subjects. The CT images were captured using the Philips Brilliance 64 CT scanner at AMC Amsterdam. The images had a voxel size of (0.3301 X 0.3301)mm, pitch of 0.3301mm and slice thickness of 0.67mm. In each case, the wrist bones and radii were initially segmented using threshold connected region growing, followed by binary closing algorithm. This intermediate result is used to initialize a Laplacian level-set segmentation growth algorithm [33]. A 3-dimensional polygon was derived from the segmented data that served as a virtual 3-dimensional model of the bone. The files were stored in the stl format and comprised of the vertices and faces. Since the number of faces and vertices in the point clouds varied, each mesh was down-sampled to 10000 points using the open source software Meshlab [34]. The training shapes were also positioned arbitrarily in space and had to be translated to a common origin before creating the shape model. An advantage of down-sampling the meshes was reducing the computation time while creating the shape model.

4.2. Experiments

In this section, the experiments conducted will be outlined. Three sets of experiments were carried out:

- 1. Model Complexity (Number of SPHARM Components).
- 2. Number of Modes of the Statistical Shape Model.
- 3. Varying scale of Gaussian Smoothing initial step size in Levenberg Marquardt optimization.

4.2.1. Model Complexity

While building the model, an important parameter to keep in mind is the L_{max} value to expand the SPHARM basis function. Models were built for the values $L_{max}=15,20,25,30$. With increasing L_{max} values, the number of coefficients increased and so did the computation time of segmenting. Hence, based on eyeballing, an L_{max} value of 20 was chosen for conducting the experiments.

4.2.2. Number of modes

A leave one out approach (LOOC) was adopted, where 19 out of 20 shapes were used to create SSM. Subsequently, the model was fit to the new bone image using n modes of the highest variance. The error measure taken was the mean Euclidean distance between the reference shape and the surface points predicted by the model. The experiments were conducted for N = 4,7,9,13 modes of variation.

4.2.3. Gaussian Scale of Smoothing and Initial Step Size in LM algorithm

Since the metric optimized used the intensity information of the 3D CT image, a Gaussian blurring was applied to the image prior to calculating the first order derivative using the Sobel Matrix. The resulting image is shown in Figure (4.1). Since the Transformation optimization and the Shape optimization is carried out separately, multiple experiments were first carried out for optimizing the transformation parameters at different values of the width of the Gaussian kernel σ . Particularly, σ was varied between the values [1,5] for interval s=0.5, giving us nine different scales. The initial step size δ for the shape optimization alone was varied between the values of $[0.5,0.7,0.9]*sqrt(\lambda)$, where λ is the Initial value of the Levenberg-Marquardt parameter, a positive scalar.

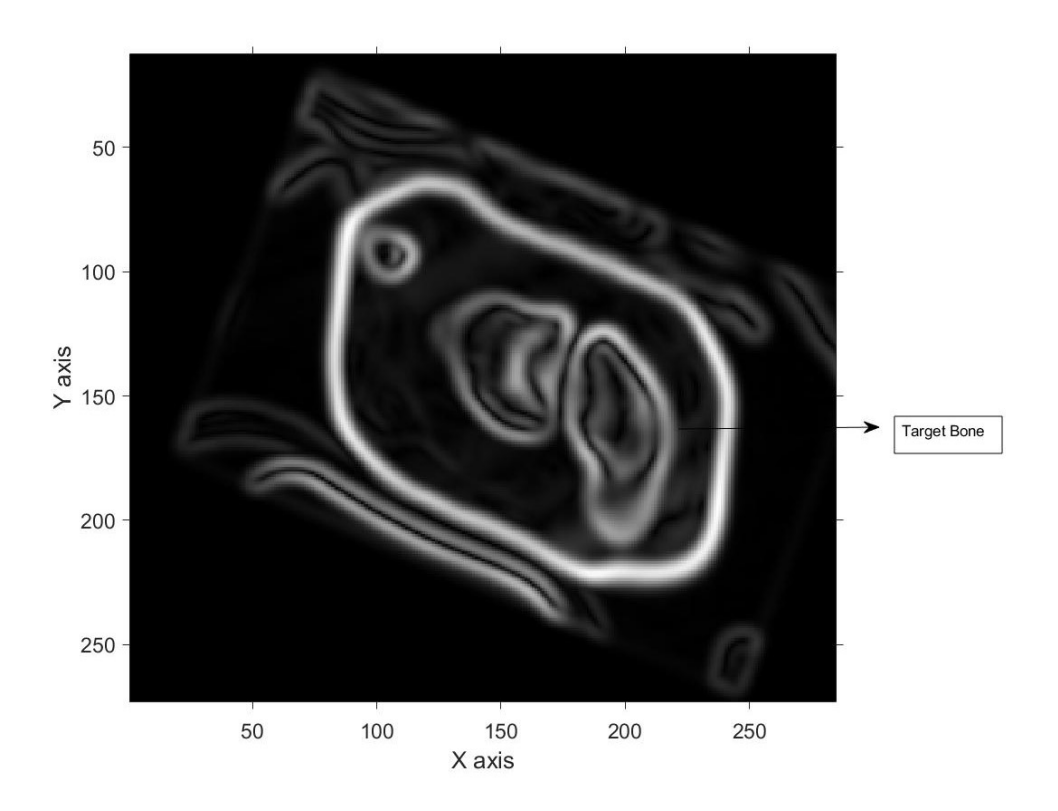


Figure 4.1: Gradient Magnitude.

4.3. Segmentation Evaluation

DICE coefficient

The Sørensen–Dice index [35] is a statistical tool used for measuring the overlap between two dataset. The similarity operation is expressed in terms of vector operations over binary vectors A and B:

$$s_v = \frac{2 * |A \cap B|}{|A| + |B|} \tag{4.1}$$

In our project, binary vectors A and B represent the modified shape and the ground truth. The DICE coefficient lies in the range [0,1], with 1 representing complete overlap of the two vectors and 0 representing complete separation of the two vectors.

Distance Map

Another useful way to quantify the segmentation accuracy is to create a distance map between the ground truth and the final shape model. The k nearest neighbours can be estimated between the two meshes and a Euclidean distance can be estimated.

4.4. Results

4.4. Results

Post registration of the training dataset, PCA was applied to it and the distribution of the scaphoid can be seen in Figure (4.1). Here, the first two modes of variation, varying from $\pm 2\sigma$ are shown, with the column in the middle representing the mean shape.

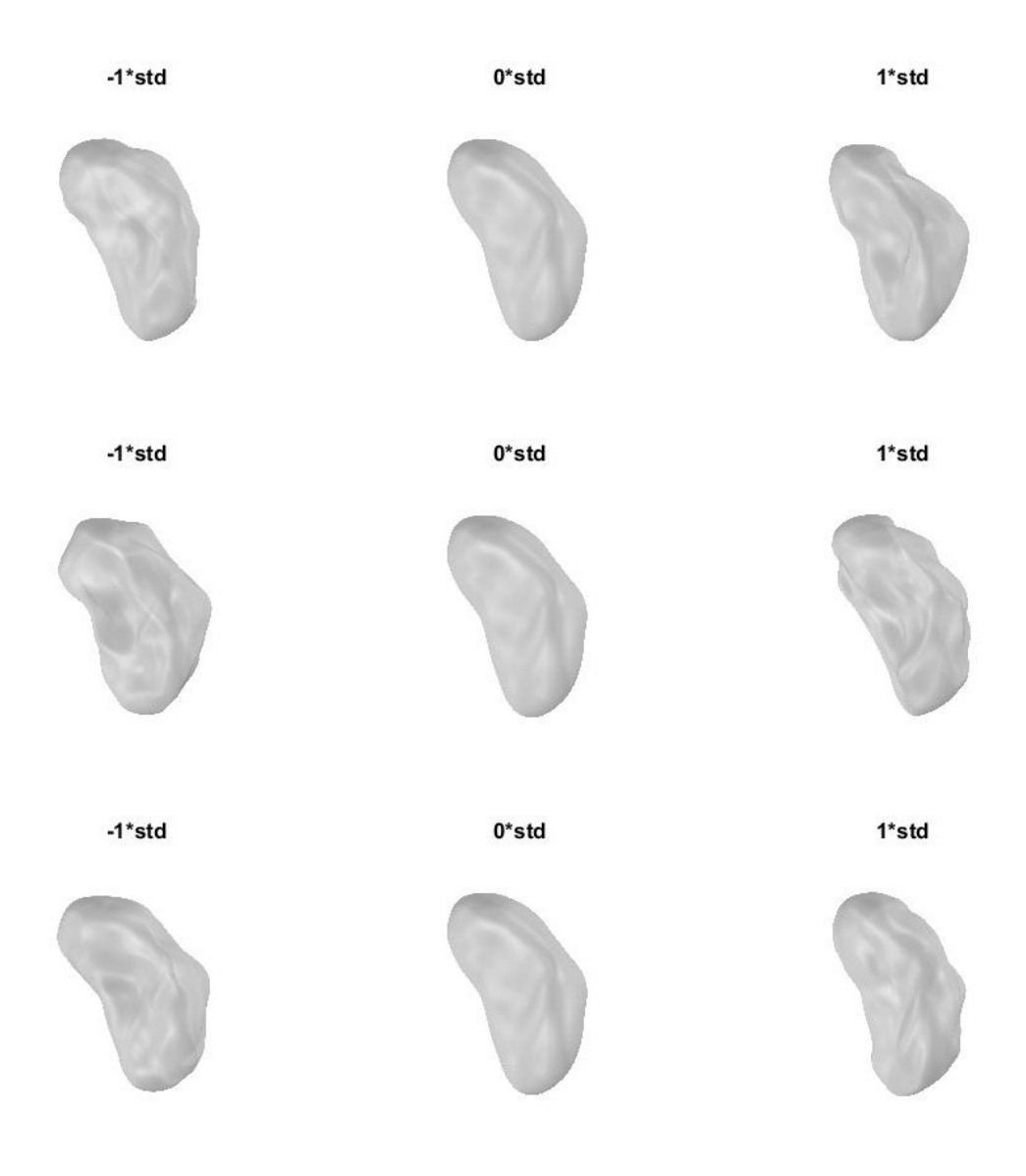


Figure 4.2: First two modes of variation post FOE alignment.

The resulting model can also be described by the percentage variation and the cumulative percentage of variance explained by each principal component, as shown in Figure (4.3) respectively. This plot became the basis for selection of number of modes for model fitting. The topmost horizontal intersection at 98% of the total variation in Figure (4.3) shows that, using a maximum of 13 modes out of the total 18 can be useful for altering the model to fit the test bone. Varying these modes for a set of σ values, the model was fit to the new image.

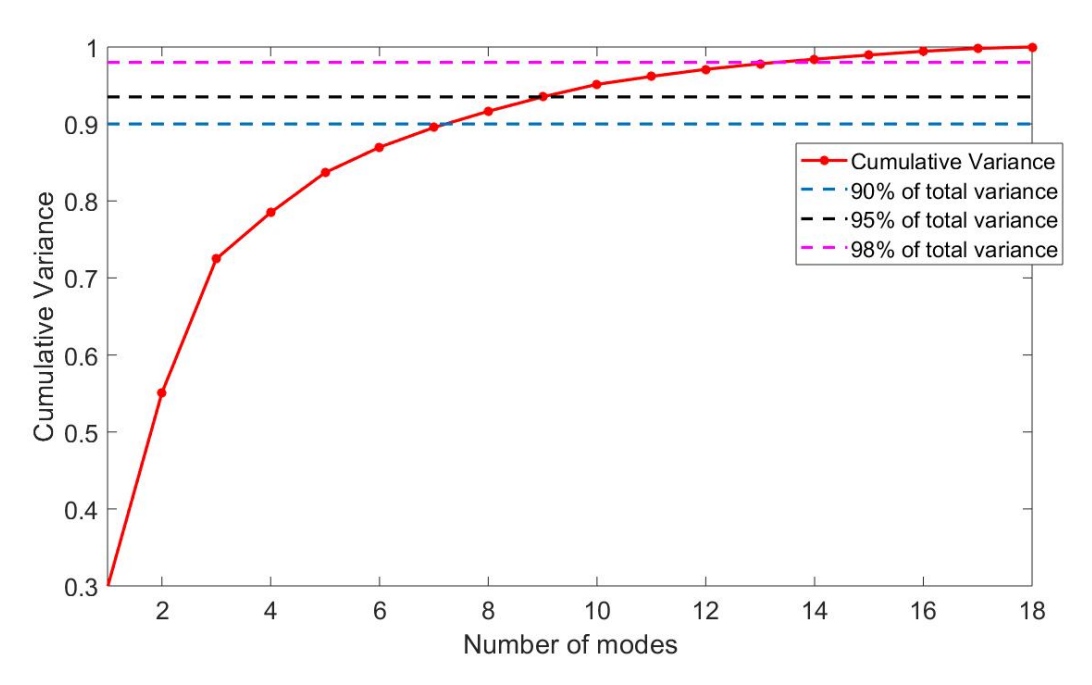


Figure 4.3: Variance explained by each principal component for the first shape and the Cumulative variance explained by each principal component.

In the model fitting process, key factors are function tolerance, step tolerance, the step size difference and the damping factor. In LM optimization, the damping factor λ controls the speed of convergence. The step tolerance is the lower bound on the size of the step.

For Pose Optimization, the step tolerance, function tolerance and damping factor were kept constant while, the step size and σ values were varied. Arbitrary step sizes were chosen and the optimum position of the model was estimated for varying values of sigma.

The pose parameters that gave a distinct change and moved the shape towards the ground truth was chosen. These values were then kept fixed and the shape parameters were obtained for different σ and step sizes. The final pose parameters were obtained after 3 iterations and during each iteration, the parameters were updated individually. This means, given there were six parameters in total, each iteration contained six sub-iterations. On an average, this process took 10 minutes to complete.

4.4.1. Shape Optimization

The number of iterations to optimize the shape is determined by the number of modes chosen. In case of Shape Optimization, the step sizes were chosen such that, they lay between the $\pm 2\lambda$ bounds, for the following values of s:

- 1. $0.5 * \sqrt{(\lambda)}$
- 2. $0.7 * \sqrt{(\lambda)}$
- 3. $0.9 * \sqrt{(\lambda)}$

The Gaussian scale was varied between the values $\sigma = 2, 2.5, 3, 3.5, 4$.

Given an L_{max} of 20 was chosen, the total number of SPHARM coefficients were 441. These coefficients are present in the parametric space. In order to compute the distance between the final model and the ground-truth, these coefficients had to be represented in the cartesian coordinate system.

4.4. Results 31

Figures (4.4) is an example of the transition of the mean model towards the ground truth. In the below figure, three different contours, the ground truth, the mean model and the deformed shape can be visualized.

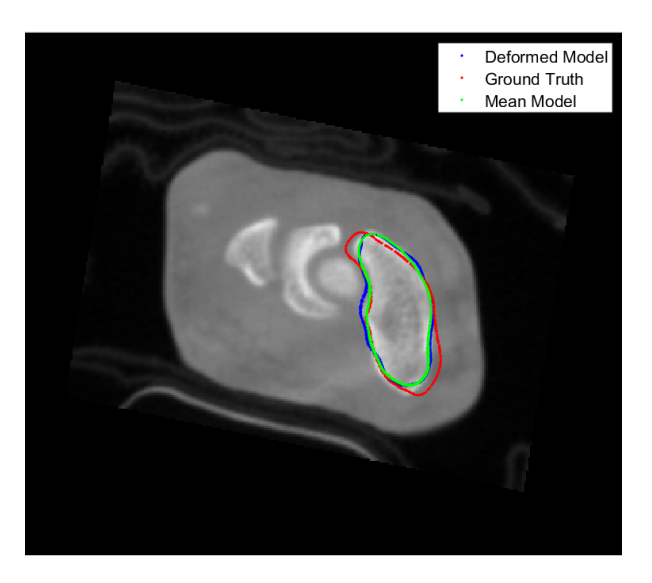


Figure 4.4: Modes N = 9, σ = 2.5, s = 0.7* $\sqrt{\lambda}$.

A Distance metric has been used to observe the transition of the mean model to the ground truth for varying values of the Gaussian Scale Sigma. Figures (4.5 - 4.6) show the mean error of the model from the ground truth for a step size of $s=0.5*\sqrt(\lambda)$ and $s=0.7*\sqrt(\lambda)$ the number of modes were varied for N=7(90%),9(95%) and 13(98%) and the Gaussian scale is varied for $\sigma=1.5$

- 1. 2
- 2. 2.5
- 3. 3
- 4. 3.5
- 5. 4

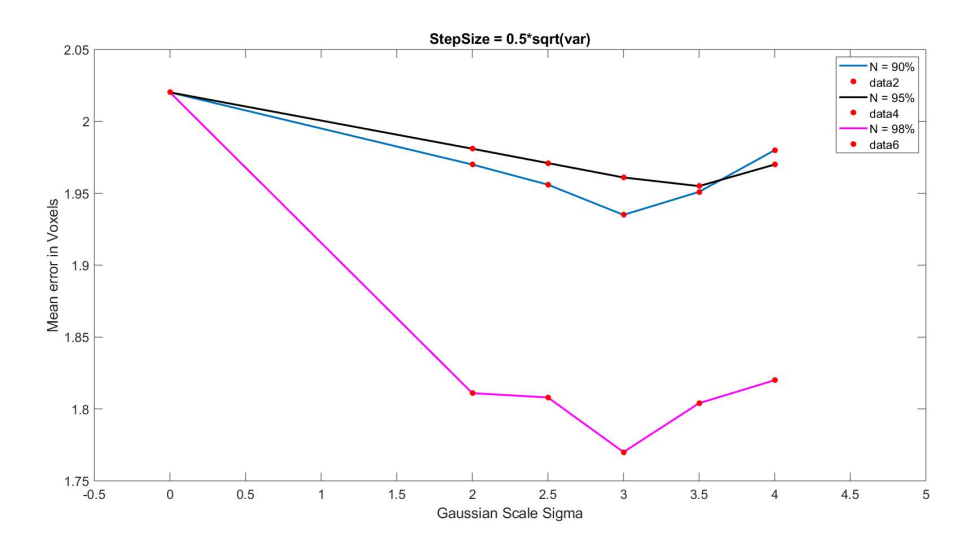


Figure 4.5: Modes N = 7, 9, 13 for a fixed step size of $0.5 * \sqrt{(\lambda)}$.

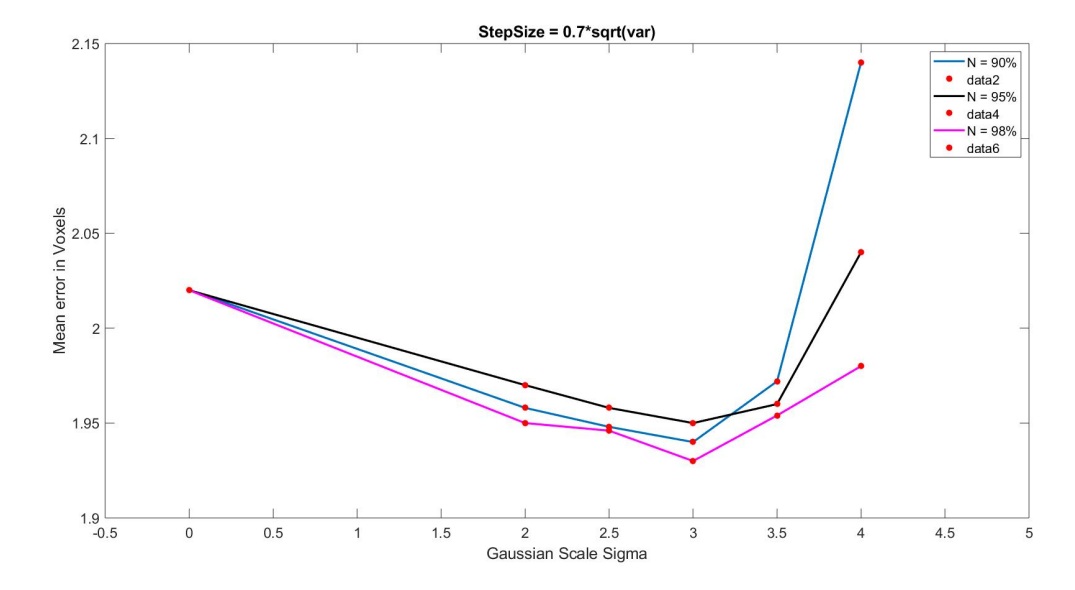


Figure 4.6: Modes N = 7, 9, 13 for a fixed step size of $0.7 * \sqrt{(\lambda)}$.

Figure (4.7) shows the binarized region within the ground truth and the the deformed model. The DICE coefficient, given below each image indicates the percentage of similarity between the two regions.

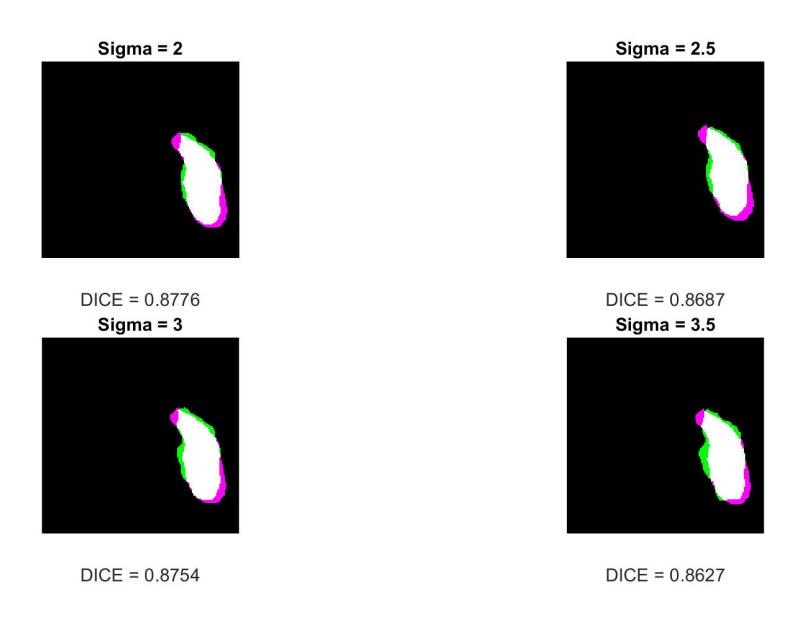


Figure 4.7: DICE coefficient for N = , σ = 2, 2.5, 3, 3.5, s = 0.7* $\sqrt{\lambda}$.

Figure (4.8) shows the point cloud structure of the reference bone shape and the deformed model from the side view . Figure (4.9) is a comparison of the reference shape and the deformed model. As it can be seen, not all details of the scaphoid structure could be accommodated in the final segmented volume.

4.4. Results

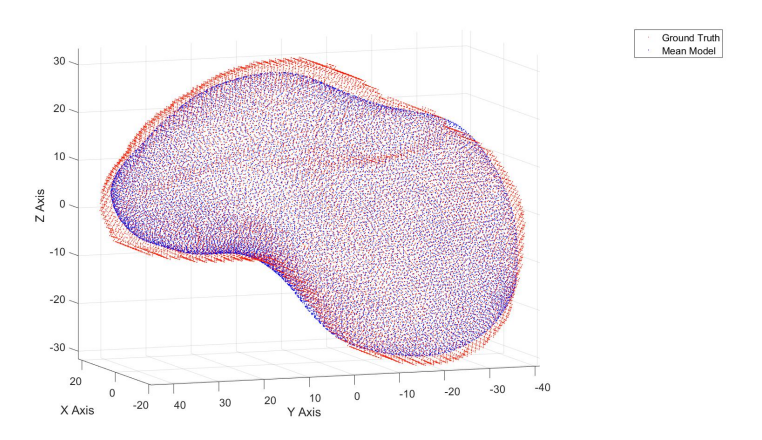
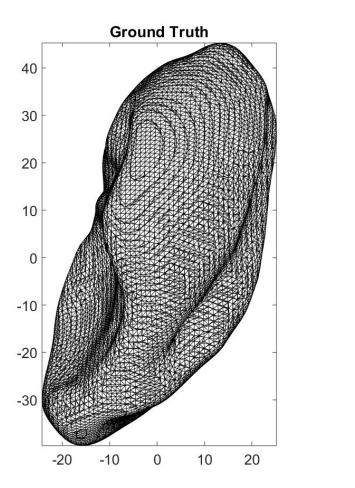


Figure 4.8: Side View of the Reference Shape and the final Deformed Model at $\sigma=3$.



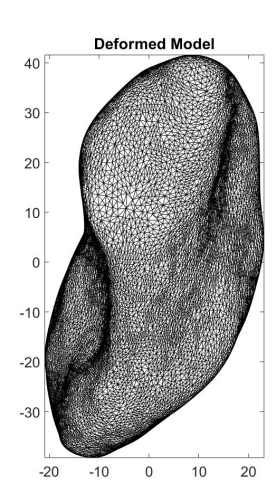


Figure 4.9: Reference Shape and Deformed model at σ = 3.

Discussion and Conclusion

Segmentation of Orthopaedic Images is of utmost importance in Computer Aided Orthopaedic Surgeries. Currently, the commonly used techniques are Level Sets and Active Shape Models. However, in order to exclude manual landmarking of the training images and also, to reduce the time taken to segment the images, a spherical coordinate system based technique can be taken into consideration. In this project, a Statistical Shape Model using spherical harmonics has been implemented.

5.1. Analysis

At lower scales of blurring, there was no distinct change in the model from the initial geometry. However, with increasing values of σ , the shape tended to become very irregular. A possible reason is due to the incorrect positioning of the shape model. Since, the model position optimization was not highly accurate, the contours of the model tended to encroach areas of the neighbouring bones of similar texture. This led to erratic behaviour of the shape model during the iterative process, at times leading the algorithm to fail in convergence.

This in turn compromised the Shape optimization process. Generally, the shape must not deviate from the geometry of the mean model with increasing scale of the Gaussian filter. However, in our case, the shape deformed into a highly irregular structure. This can be caused due to presence of coarser edge information. The high frequency information along with background noise tend to get eliminated with increased smoothing. Furthermore, increasing the blur scale also reduces the effectiveness of localization. This disrupts the model from converging to the true edge of the test image.

While building the model, not all training shapes were of the same size. Some of the training scaphoids were significantly larger than others. This affected the final shape of the model. Next, during model fitting, the scale was kept constant and was not varied in the optimization process. This parameter might have also affected the final result, as the model contour and the gradient edges might not have coincided during the transformation and shape optimization process. From Figure (4.8) shown in section (4.4.1), we can observe that, there is a considerable gap between the reference shape and the deformed model. This can lead to failure in convergence of the mean model towards the edges of the test scaphoid.

5.2. Recommendation

To overcome the limitations seen above, the following steps can be taken into account. Instead of a first order Gaussian derivative, a possible option is to use Laplacian of the Gaussian (LOG) filter in the metric, to calculate the inner product. One of the reasons is, the second order derivatives have a stronger response to finer details and isolated points in the image. However, there is no effective

criterion to select/ determine the blurring scales that can give the best result for segmentation [36].

While building the shape model, time taken for model construction was the only criteria used for choosing the maximum degree of the SPHARM function. An alternative can be, to use the Akaike information criterion (AIC) or Rissanen Minimum Description Length, as suggested by Melinska *et. al.*, [37]. Even though the time taken to build the shape model will increase, the accuracy of model fitting will also increase as more details will be contained in the model.

Since the SPHARM model is variant to rotation, the transformation and shape optimization had to be carried out in two different steps, thereby reducing the accuracy of segmentation process. Kazhdan *et.al.* [38], have proposed a framework to obtain rotation invariant shape descriptors, wherein the frequency information of the training shapes is used for image registration. Furthermore, combining the texture information (as discussed in chapter 2) into the shape model can increase the chances of accurate segmentation of the organ of interest.

One of the effective methods for coordinate system transformation can be pf use is the iterative closest point (ICP) algorithm.

5.3. Conclusion

The performance of the algorithm was less satisfactory than expected, as the transformation parameters couldn't be optimized effectively. The time duration has considerably reduced in comparison to the methods used previously while segmenting the wrist bone (Level sets). There was no significant difference between the final shape models, with change in the Gaussian scale. However, the time taken to carry out the entire process was considerably reduced compared to the time taken to segment the ground truth. From these points, we can conclude that the above framework can be used as a source to improve the model building as well as the segmentation flow.

Bibliography

- [1] L. Joskowicz and E. J. Hazan, *Computer aided orthopaedic surgery: incremental shift or paradigm change?* Medical image analysis **33**, 84 (2016).
- [2] T. Heimann and H.-P. Meinzer, *Statistical shape models for 3d medical image segmentation: a review,* Medical image analysis **13**, 543 (2009).
- [3] I. Despotović, B. Goossens, and W. Philips, *Mri segmentation of the human brain: challenges, methods, and applications,* Computational and mathematical methods in medicine **2015** (2015).
- [4] A. Zhang, A. Gertych, and B. J. Liu, *Automatic bone age assessment for young children from newborn to 7-year-old using carpal bones,* Computerized Medical Imaging and Graphics **31**, 299 (2007).
- [5] M. van de Giessen, M. Foumani, F. M. Vos, S. D. Strackee, M. Maas, L. J. Van Vliet, C. A. Grimbergen, and G. J. Streekstra, *A 4d statistical model of wrist bone motion patterns,* IEEE transactions on medical imaging **31**, 613 (2012).
- [6] E. M. A. Anas, A. Rasoulian, A. Seitel, K. Darras, D. Wilson, P. S. John, D. Pichora, P. Mousavi, R. Rohling, and P. Abolmaesumi, *Automatic segmentation of wrist bones in ct using a statistical wrist shape* + *pose model*, IEEE transactions on medical imaging **35**, 1789 (2016).
- [7] R. Malladi, J. A. Sethian, and B. C. Vemuri, *Shape modeling with front propagation: A level set approach*, IEEE transactions on pattern analysis and machine intelligence **17**, 158 (1995).
- [8] M. B. Stegmann and D. D. Gomez, *A brief introduction to statistical shape analysis,* Informatics and mathematical modelling, Technical University of Denmark, DTU **15** (2002).
- [9] T. F. Cootes, G. J. Edwards, and C. J. Taylor, *Active appearance models*, IEEE Transactions on pattern analysis and machine intelligence **23**, 681 (2001).
- [10] A. Kelemen, G. Székely, and G. Gerig, *Elastic model-based segmentation of 3-d neuroradiological data sets*, IEEE Transactions on medical imaging **18**, 828 (1999).
- [11] M. Styner, I. Oguz, S. Xu, C. Brechbühler, D. Pantazis, J. J. Levitt, M. E. Shenton, and G. Gerig, Framework for the statistical shape analysis of brain structures using spharm-pdm, The insight journal, 242 (2006).
- [12] I. B. Tutar, S. D. Pathak, L. Gong, P. S. Cho, K. Wallner, and Y. Kim, *Semiautomatic 3-d prostate segmentation from trus images using spherical harmonics,* IEEE transactions on medical imaging **25**, 1645 (2006).
- [13] S. Eck, S. Wörz, K. Müller-Ott, M. Hahn, A. Biesdorf, G. Schotta, K. Rippe, and K. Rohr, *A spherical harmonics intensity model for 3d segmentation and 3d shape analysis of heterochromatin foci,* Medical image analysis **32**, 18 (2016).
- [14] Y. Fu, S. Liu, H. H. Li, and D. Yang, *Automatic and hierarchical segmentation of the human skeleton in ct images*, Physics in Medicine and Biology **62**, 2812 (2017).
- [15] L. Wang, Y. Gao, F. Shi, G. Li, K.-C. Chen, Z. Tang, J. J. Xia, and D. Shen, *Automated segmentation of dental cbct image with prior-guided sequential random forests,* Medical physics **43**, 336 (2016).
- [16] C. Chu, C. Chen, L. Liu, and G. Zheng, *Facts: fully automatic ct segmentation of a hip joint,* Annals of biomedical engineering **43**, 1247 (2015).
- [17] J. S. Athertya and G. S. Kumar, *Automatic segmentation of vertebral contours from ct images using fuzzy corners*, Computers in biology and medicine **72**, 75 (2016).

38 Bibliography

[18] S. Chen, D. M. Lovelock, and R. J. Radke, *Segmenting the prostate and rectum in ct imagery using anatomical constraints*, Medical image analysis **15**, 1 (2011).

- [19] S.-H. Cha and S. N. Srihari, *On measuring the distance between histograms,* Pattern Recognition **35**, 1355 (2002).
- [20] Y. Ge, D. Yang, J. Lu, B. Li, and X. Zhang, *Active appearance models using statistical characteristics of gabor based texture representation*, Journal of Visual Communication and Image Representation **24**, 627 (2013).
- [21] T. Ojala, M. Pietikäinen, and D. Harwood, *A comparative study of texture measures with classification based on featured distributions,* Pattern recognition **29**, 51 (1996).
- [22] E. Tekeli, M. Çetin, and A. Erçil, Shape and data driven texture segmentation using local binary patterns, in Signal Processing Conference, 2007 15th European (IEEE, 2007) pp. 1442–1446.
- [23] T. Ahonen, A. Hadid, and M. Pietikainen, *Face description with local binary patterns: Application to face recognition*, IEEE transactions on pattern analysis and machine intelligence **28**, 2037 (2006).
- [24] G. Gonzáleza and B. Escalante-Ramırezb, *Knee cartilage segmentation using active shape models and local binary patterns*, in *Proc. of SPIE Vol*, Vol. 9138 (2014) pp. 91380K–1.
- [25] M. J. Mohlenkamp, A user's guide to spherical harmonics, may 10, 2010, .
- [26] M. LLC, Spherical coordinate system, (2007).
- [27] L. Shen and F. Makedon, *Spherical mapping for processing of 3d closed surfaces,* Image and vision computing **24**, 743 (2006).
- [28] L. Shen, H. Farid, and M. A. McPeek, *Modeling three-dimensional morphological structures using spherical harmonics*, Evolution: International Journal of Organic Evolution **63**, 1003 (2009).
- [29] L. Shen and M. K. Chung, Large-scale modeling of parametric surfaces using spherical harmonics, in 3D Data Processing, Visualization, and Transmission, Third International Symposium on (IEEE, 2006) pp. 294–301.
- [30] M. Fang, G. Yue, and Q. Yu, *The study on an application of otsu method in canny operator,* in *International Symposium on Information Processing (ISIP)* (Citeseer, 2009) pp. 109–112.
- [31] H. Gavin, *The levenberg-marquardt method for nonlinear least squares curve-fitting problems,* Department of Civil and Environmental Engineering, Duke University, 1 (2011).
- [32] M. LLC, Research gate, a 3d rotation as a sequence of yaw, pitch and roll, (2016).
- [33] J. Vroemen, J. Dobbe, R. Jonges, S. Strackee, and G. Streekstra, *Three-dimensional assessment of bilateral symmetry of the radius and ulna for planning corrective surgeries,* The Journal of hand surgery **37**, 982 (2012).
- [34] P. Cignoni, M. Callieri, M. Corsini, M. Dellepiane, F. Ganovelli, and G. Ranzuglia, *Meshlab: an open-source mesh processing tool.* in *Eurographics Italian Chapter Conference*, Vol. 2008 (2008) pp. 129–136.
- [35] A. A. Taha and A. Hanbury, *Metrics for evaluating 3d medical image segmentation: analysis, selection, and tool, BMC medical imaging* **15**, 29 (2015).
- [36] M. Basu, *Gaussian-based edge-detection methods-a survey,* IEEE Transactions on Systems, Man, and Cybernetics, Part C (Applications and Reviews) **32**, 252 (2002).
- [37] A. U. Melinska, P. Romaszkiewicz, J. Wagel, M. Sasiadek, and D. R. Iskander, *Statistical, morphometric, anatomical shape model (atlas) of calcaneus, PloS one* **10**, e0134603 (2015).
- [38] M. Kazhdan, T. Funkhouser, and S. Rusinkiewicz, *Rotation invariant spherical harmonic representation of 3 d shape descriptors,* in *Symposium on geometry processing,* Vol. 6 (2003) pp. 156–164.